

Equilibrium and non-equilibrium furanose selection in the ribose isomerisation network

Avinash Vicholous Dass,[†] Thomas Georgelin,[†] Frances Westall,[†] Frédéric Foucher,[†] Paolo De Los Rios,[§] Daniel Maria Busiello,[§] Shiling Liang,[§] and Francesco Piazza^{*,[⊥]}

[†]*Centre de Biophysique Moléculaire, CNRS-UPR4301, Rue C. Sadron, 45071, Orléans, France*

[‡]*Department of Physics, Ludwig Maximilians University, Amalienstr. 54; D-80799 München, Germany*

[¶]*Laboratoire de Réactivité de Surface, UMR 7197, Sorbonne Université, Paris, France.*

[§]*Institute of Physics, School of Basic Sciences, Ecole Polytechnique Fédérale de Lausanne - EPFL, Lausanne, CH-1015, Switzerland*

^{||}*Institute of Bioengineering, School of Life Sciences, Ecole Polytechnique Fédérale de Lausanne, - EPFL, Lausanne, CH-1015, Switzerland*

[⊥]*Université d'Orléans and Centre de Biophysique Moléculaire, CNRS-UPR4301, Rue C. Sadron, 45071, Orléans, France*

E-mail: Francesco.Piazza@cns-orleans.fr

Abstract

The exclusive presence of β -D-ribofuranose in nucleic acids is still a conundrum in prebiotic chemistry, given that pyranose species are substantially more stable at equilibrium. However, a precise characterisation of the relative furanose/pyranose fraction

at temperatures higher than about 50°C is still lacking. Here, we employ a combination of NMR measurements and statistical mechanics modelling to predict a population inversion between furanose and pyranose at equilibrium at high temperatures.

More importantly, we show that a steady temperature gradient may steer an open isomerisation network into a non-equilibrium steady state where furanose is boosted beyond the limits set by equilibrium thermodynamics. Moreover, we demonstrate that nonequilibrium selection of furanose is maximum at optimal dissipation, as gauged by the temperature gradient and energy barriers for isomerisation. The predicted optimum is compatible with temperature drops found in hydrothermal vents associated with extremely fresh lava flows on the seafloor.

Introduction

Stabilisation and reactivity of sugar formation is an essential factor in the prebiotic scenario of “RNA world”,¹ in particular the phosphorylation and glycosylation of D-ribose ($C_5H_{10}O_5$) that comprise RNA. As is the case with all carbohydrates, ribose has been synthesised by polymerisation of formaldehyde in abiotic conditions from the formose reaction,²⁻⁴ although in very minor quantities.⁵ After synthesis the ribose molecule is unstable in aqueous solution.⁶ For example, at pH 7 and 90°C, its half-life is about 10 h.⁷ Despite its lack of stability, ribose is the exclusive constituent of the carbohydrate part of RNA in its β -D-ribofuranose form (hereafter simply furanose). At thermal equilibrium, at room temperature and ambient pressure, this enantiomer represents only 12 % of all ribose molecules in solution.⁸ Thus, it is of paramount importance to explain the exclusive incorporation of β -D-ribofuranose in RNA. There are many potential causes for this, ranging from incorporation due to a specific chemical process during phosphorylation or glycosylation, or perhaps due to specific physicochemical conditions on the early Earth that led to a significant increase in the proportion of furanose.

Indeed, the phosphorylation of ribose could favour a specific enantiomer. It has been

shown that the glycosylation of ribose under the α -furanose form can lead to the formation of β -furanose nucleosides.⁹ In order to solve the problems of stability and enantiomeric structure, some studies have analysed the ability of ribose to form borate or silicate complexes that are more stable in solution.^{10,11} Furthermore, theoretical studies have also shown that silicate/ribose complexes would be formed exclusively from the furanose form because, with this structure, the HO-C-C-OH dihedral angle is sufficiently small to allow the formation of a planar five-membered ring.¹² The silicate or borate scenarios have shown the high potential of inorganic/organic interactions, although the presence of significant borate on the early Earth is unclear.¹³ Moreover, since coordination processes seem to have an impact on isomerisation, it is possible that thermal effects at equilibrium could also have an impact on these processes and on the anomeric ratios. Thus, it is important to investigate the effect of temperature on ribose isomerisation at thermal equilibrium. This aspect has not yet been thoroughly studied, despite the fact that temperatures on the primitive Earth, at least at the rock/water interface where prebiotic reactions were taking place, were likely higher than 50°C.^{13,14} It is to be noted, however, that the environments where prebiotic chemical reactions thrived,¹³⁻¹⁵ such as hydrothermal vents and their immediate vicinity, were by no means at thermal equilibrium. Most probably, chemical reaction networks proceeded under the action of high, steady gradients of temperature, pH¹⁶ and chemical activity of key molecular species, such as water.^{13,15,17-20}

It is well known that open chemical systems²¹ driven far from equilibrium may settle in non-equilibrium steady states (NESS) that bear little resemblance with equilibrium ones.²² A well-known example are chemical transformations that proceed thanks to catalysers, such as enzyme catalysis in biology, where substrate and product species are kept at fixed concentration (chemostatted) by an external source of energy.²³ The work done on the system to enforce the required chemical potential difference leads to sustained dissipative currents that steer the chemical transformations away from equilibrium.²⁴ In more chemical terms, a NESS should be considered as a regime of sustained kinetic control, with reference to

the well-known concept of transient kinetic control of chemical reactions, as opposed to so-called thermodynamic control regime, that is, thermodynamic equilibrium.²⁵ More recently, the subtle effects of steady temperature gradients on chemical reaction networks have been brought to the fore, especially as regards the coupling of sustained mass currents in physical space and chemical currents in state space, which, based on kinetic rules, may push the steady-state molar fraction of certain chemical species away from equilibrium values.^{26,27}

In this paper, we focus on a coarse-grained chemical reaction networks describing D-ribose isomerisation. Our main working hypothesis is that β -furanose could be ultra-stabilised under steady non-equilibrium conditions beyond the limits imposed by equilibrium thermodynamics. In order to investigate this idea and quantify the necessary conditions in terms of the unknown kinetic parameters, the first step was to accurately characterise the anomeric ratios at equilibrium as a function of temperature through NMR. The data are fitted to a simple equilibrium model, solved under the constraint of detailed balance. The first remarkable finding is that, in view of the large entropic degeneracy associated with sub-conformations of α - and β -furanose, the populations of these high-energy species are predicted to increase with temperature, eventually leading to a population inversion at high temperature.

Equipped with the thermodynamic parameters derived from our experiments, in the second part of the paper we report a theoretical exploration of D-ribose isomerisation under non-equilibrium conditions, more specifically under the action of an applied steady gradient of temperature. In this setting, we show that mass currents sustained by the temperature gradient can couple to chemical transformation steps and drive the system into a steady state where the most unstable furanose species is stabilised beyond the equilibrium limits. Remarkably, we predict this kind of non-equilibrium population inversion to be potentially more effective than that observed at equilibrium at high temperatures. This is because much higher fractions of furanose may be produced if the same thermal energy is injected in the form of a gradient, accompanied by dissipation proceeding along specific relaxation pathways determined by kinetic rules. These predictions are complemented by detailed calculations

and quantified by simple, transparent analytical conditions involving energy barriers for chemical transformations, the Damköhler number and the entropy production rate of the system.

NMR characterisation of D-ribose isomerisation at thermal equilibrium

In order to investigate the behaviour of ribose isomerisation in solution at equilibrium at increasing temperatures, we carried out ^{13}C NMR experiments. This quantitative technique allows unambiguous identification of each anomeric form of ribose by studying the C1 signal of ribose (see supplementary information for more details). In the following, we denote with $\alpha\text{F}, \beta\text{F}$ and $\alpha\text{P}, \beta\text{P}$ the two enantiomers of furanose (F) and pyranose (P), respectively. We recorded two different sets of spectra. The first set was collected in the temperature range 10-80°C in pure water. A second set of measurements were conducted in the temperature range 10-25°C in simulated Hadean sea water,¹ with the purpose of investigating isomerisation at equilibrium in the presence of relevant saline conditions (see also supplementary material).

The thermal behaviour of D-ribose isomerisation at the resolution of our NMR experiments is governed by the energy (enthalpy) differences between different states, as well as by the degeneracies associated with the different sub-structures of the four main conformations,²⁹ which cannot be resolved in our spectra. Based on these considerations, we can formulate a simple equilibrium model as depicted in Fig. 1 (left panel), that involves the linear conformation and the four ring species, βP , αP , βF , αF . These are labelled with integers from 0 to 4, respectively, as illustrated in Fig. 1. According to the above considerations, the transition rates can be written as the product between a temperature-independent geometric (i.e. entropic) velocity and an Arrhenius-like term, gauging the thermal activation of the transition. Let us denote with x_i ($i = 0, 1, \dots, 4$) the relative concentration (molar fraction)

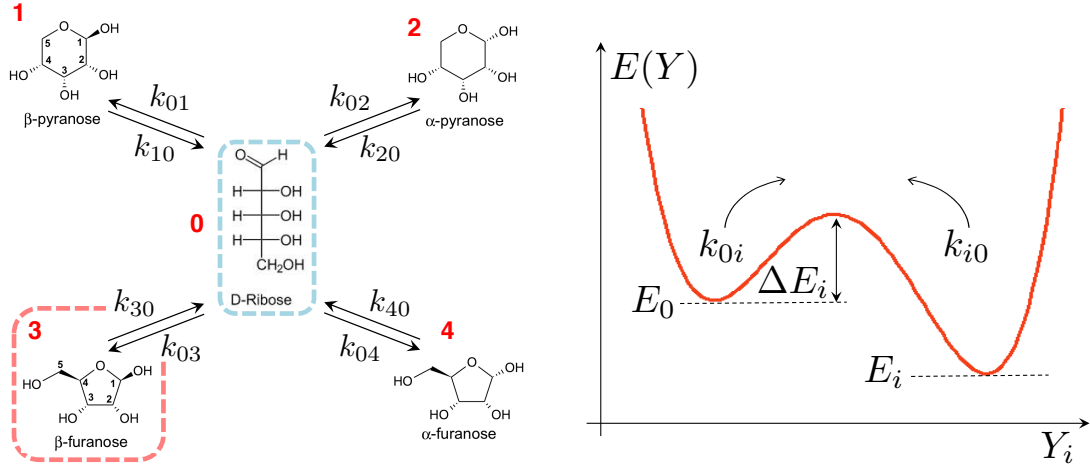


Figure 1: **Scheme of the D-ribose isomerisation reaction network and model energy landscapes.** The two pyranoses (α and β) and the two furanoses (α and β) are in equilibrium at a given temperature and pressure with the high-energy linear conformation. Right: scheme of the Gibbs free energy landscape along a representative reaction coordinate for the transition between the linear chain and the i -th anomer. The energy of the linear conformation is the highest, i.e. $E_0 > E_i \forall i$,²⁹ corresponding to a population that is undetectable in solution via NMR measurements.

of the i -th species, so that $\sum_{m=0}^4 x_m = 1$. With reference to Fig. 1 (right panel), we may thus write

$$\begin{cases} k_{0i} = k_{0i}^{\infty} e^{-\beta \Delta E_i} \\ k_{i0} = k_{i0}^{\infty} e^{-\beta(\Delta E_i + E_0 - E_i)} \end{cases} \quad (1)$$

where $\beta^{-1} = k_B T$, k_B being Boltzmann's constant. The energy of the open linear conformation is the highest, averaging about 19 kJ/mol in the gas phase.²⁹ This is confirmed by our solution measurements, where this conformation is undetectable (see supplementary information). It is not difficult to check that, in the limit $\beta E_0 \gg 1$, the stationary solution of the rate equations for the ribose isomerisation network depicted in Fig. 1 at thermal equilibrium read

$$x_i = \frac{\eta_i e^{-\beta E_i}}{\sum_{m=1}^4 \eta_m e^{-\beta E_m}} \quad i = 1, 2, \dots, 4 \quad (2)$$

where $\eta_i = k_{0i}^{\infty}/k_{i0}^{\infty}$. The degeneracy factors η_i embody the entropic contributions to the interconversion rates, so that the difference in entropy between states i and j can be computed

as $\Delta S_{ij} = k_B \log(\eta_i/\eta_j)$. These are mainly associated with the specificities of the multidimensional free-energy landscapes, including local minima corresponding to sub-conformations of each anomer that are in fast equilibrium with the main isoforms corresponding to the four detected NMR lines.

Fig. 2 shows clearly that the simple equilibrium model (2) provides an excellent de-

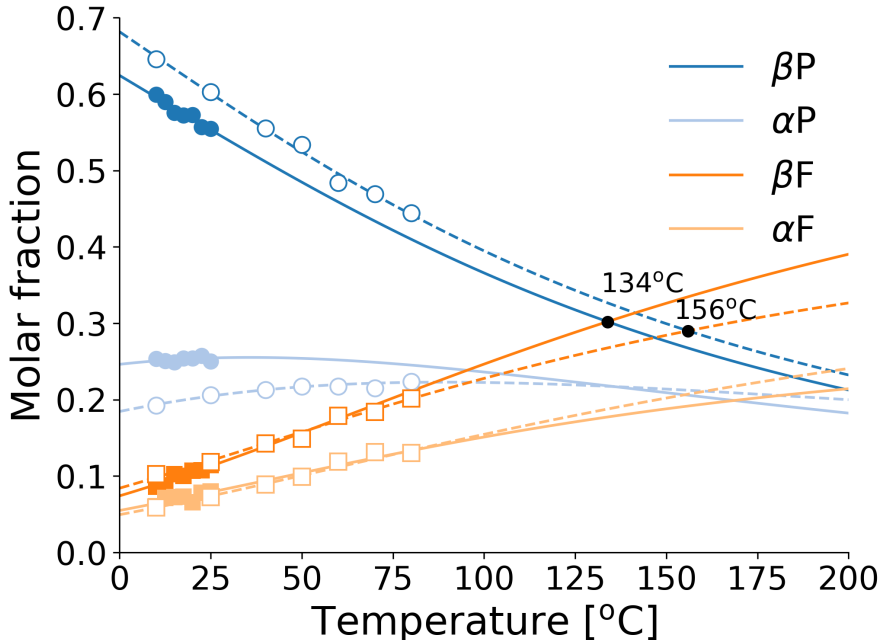


Figure 2: **Population inversions in D-ribose isomerisation network at thermal equilibrium.** The average molar fractions of the four main anomers of D-ribose are plotted versus temperature for the experiments performed in pure water (open symbols) and in Hadean model water (filled symbols, see supplementary material for more details). Lines are fits performed simultaneously with Eqs. (2) to the four anomer temperature series (see Table 1). Dashed lines: pure water, solid lines: Hadean model water. In practice, we minimised a single cost function that included a total of $4N_T$ points, where N_T is the number of temperature points considered ($N_T = 7$ for both pure and Hadean water).

scription of the NMR data as temperature increases. The first observation to be made is that the two high-energy furanose species become stabilised as temperature increases, while the equilibrium molar fractions of the more stable pyranoses decrease correspondingly. As a consequence, our analysis predicts that a series of population inversions between the high-energy species β -furanose and the two low-energy ones, α -pyranose, should occur

Table 1: Thermodynamic parameters describing the equilibrium of D-ribose isomerisation in solution at fixed temperature and pressure as estimated by fitting the equilibrium theory (2) to ^{13}C NMR data.

Species	Pure water			Hadean water		
	E_i [kJ/mol]	η_i	x_i^∞	E_i [kJ/mol]	η_i	x_i^∞
1, β -pyranose	0	0.75	0.01	0	0.39	0.01
2, α -pyranose	6.2	3.14	0.05	4.2	0.96	0.02
3, β -furanose	13.0	29.27	0.47	14.7	29.88	0.71
4, α -furanose	14.2	29.41	0.47	13.1	10.88	0.26

upon increasing the temperature. The first of these should occur at a temperature of about $k_B^{-1}(E_3 - E_2)/\log(\eta_3/\eta_2) \approx 93.2$ °C, while the β -furanose- β -pyranose inversion is predicted to occur at a temperature $k_B^{-1}(E_3 - E_1)/\log(\eta_3/\eta_1) \approx 156$ °C. Interestingly, our calculations place the first furanose-pyranose inversion at a temperature some 20 °C lower in Hadean water, at about 134 °C (see again Fig. 2).

From a thermodynamic point of view, the population inversions are explicitly related to the large entropic degeneracy associated with the furanose states. The infinite-temperature molar fractions x_i^∞ provide a clear illustration of this trend ¹. From Eq. (2), these read

$$x_i^\infty = \frac{\eta_i}{\sum_{m=1}^4 \eta_m} \quad i = 1, 2, \dots, 4 \quad (3)$$

As illustrated by the calculations reported in Table 1, equilibrium thermodynamics predicts that β -furanose will dominate at high temperatures. Its stability under given geochemical conditions is thus the only limitation to the maximum fraction of furanose that can be produced at thermal equilibrium by increasing the temperature. Interestingly, this effect is magnified in Hadean water, an environment where temperature-induced boosting of β -furanose at equilibrium appears to have been much easier (see again Table 1).

¹Even if, of course, the molecular species examined are certainly not stable beyond a certain temperature.

The furanose population can be boosted beyond equilibrium in a steady temperature gradient

Our NMR experiments have made it very clear that β -furanose is progressively stabilised at increasing temperature at thermal equilibrium. However, it is well known that typical prebiotic environments, such as hydrothermal vents and the adjacent porous sediments and chemical precipitates, were characterised by strongly non-equilibrium conditions, such as steady gradients of temperature, PH and water activity.^{13,30-33} Intriguingly, in complex systems with multiple states, it has been shown that the rate of dissipation (equivalently, the rate of entropy production) conveys key information on the *selection* of states that are favoured away from equilibrium.³⁴⁻³⁶ In more chemical terms, a given reaction network driven far from equilibrium is placed under a state of sustained kinetic control. In such conditions, the energy barriers that set the velocity of chemical transformations, which are irrelevant at equilibrium, become key in selecting the steady-state populations.

Taken together, in the context of D-ribose isomerisation kinetics, the above considerations prompt the question whether high-energy furanose species could be further stabilised under steady non-equilibrium conditions, such as an imposed temperature gradient, beyond the limits imposed by equilibrium thermodynamics. The in-depth, quantitative analysis of the thermodynamic equilibrium properties performed in the first part of this study enables us to investigate this question from the vantage point of a model parameterised on solid experimental evidence.

As proposed in a recent work,²⁶ a simple way to examine a chemical reaction network under the action of a steady temperature gradient is to replicate the same system in two separate compartments, each thermalised at a different temperature, and able to exchange reactants as dictated by specific transport rates (see Fig. 7). Furthermore, with no loss of generality, we can coarse-grain the kinetics by letting the two pyranoses coalesce into a single low-energy species, E_P , and likewise reunite the two furanoses in a single high-energy moiety,

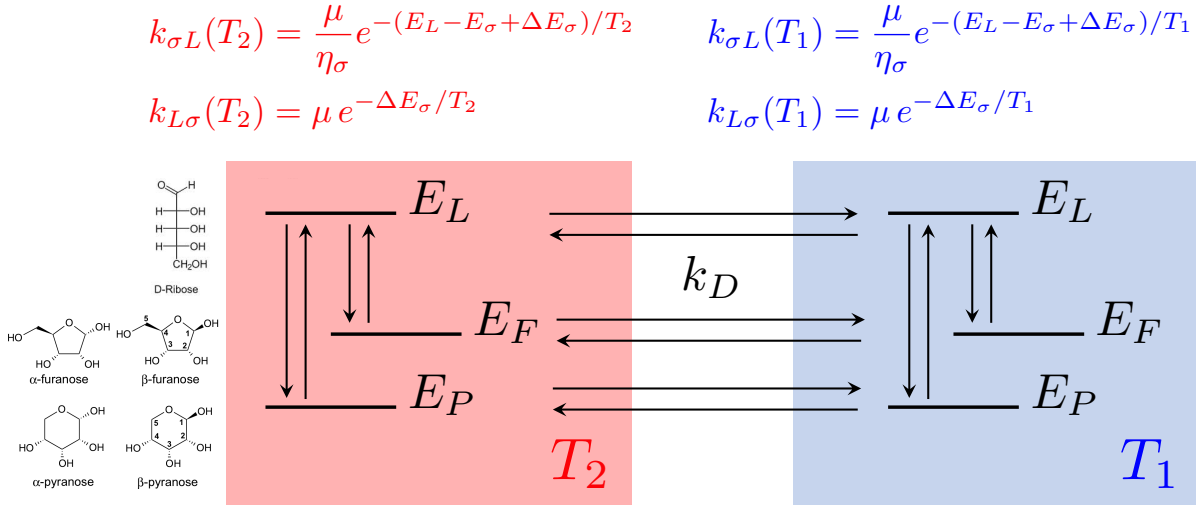


Figure 3: **Simple model of ribose isomerisation in a steady temperature gradient** ($T_2 > T_1$). The highest-energy linear species has energy E_L , αF and βF have been coalesced into the high-energy state F (energy E_F), while αP and βP are coarse-grained into the ground state (and reference energy), E_P . Chemical rates are expressed as the product of a velocity, μ , and an Arrhenius term that depends on the energy barriers ΔE_σ ($\sigma = F, P$) and include entropic degeneracy factors, η_σ , in accordance with our experimental findings.

E_F . The third species represents the open chain – the high-energy transition state, E_L . For simplicity, mass exchange (e.g. convection, diffusion) is described by a single transport rate, k_D .

In a system where chemical reactions and transport are coupled, the central physical parameter is the ratio of the respective characteristic rates. If D denotes the typical molecular diffusion coefficient of reactants, ℓ some relevant dimension of interest and μ the typical velocity of chemical transformations (see again Fig. 7), then the key parameter is known as the Damköhler number,³⁷ $\text{Da} = \mu/D\ell^2 = \mu/k_D$. This parameter measures the relative time scale of kinetic effects with respect to mass transport and thus offers a single expedient gauge for the degree of coupling between the kinetics of chemical transformations and the transport of reactants and products. In the fast reaction limit, $\text{Da} \gg 1$, transport is not swift enough to couple molecular species that undergo chemical transformations in separate compartments. Therefore, in the stationary state each box settles at thermal equilibrium at its own temperature.

When transport becomes faster, as happens for example in the presence of strong convective currents in the vicinity of hydrothermal vents,³⁸ exchange of mass between the two compartments will eventually approach timescales comparable to chemical transformations. In this regime, the steady populations of reactants are no longer dictated by detailed balance. Rather, they are governed by a kinetic selection mechanism that depends on the relative values of the energy barriers, $\Delta E_F, \Delta E_P$ (see again Fig. 1 and Fig. 7) and the strength of the temperature gradient, ΔT . Simply put, the molecular species that are generated most quickly from the transition state, E_L , will be boosted beyond the equilibrium population by large dissipative mass currents sustained by the temperature gradient. Remarkably, provided the difference between the barriers is large enough, this is true irrespective of whether the fastest state is the least or the most stable at equilibrium. Fig. 4 (top) illustrates the scenario where the imposed temperature gradient leads to non-equilibrium boosting of the high-energy furanose species.

Interestingly, while the extent of non equilibrium stabilisation of furanose in terms of its excess population with respect to equilibrium for $k_D \gg \mu$ ($\text{Da} \ll 1$) is controlled essentially by the temperature gradient, the crossover to the fast-transport limit, $\text{Da} < \text{Da}^*$, is also governed by kinetic parameters. It turns out that this can be encapsulated in a remarkably transparent formula (see supplementary material), namely

$$\text{Da}^* = \frac{1}{e^{-\Delta E_F/k_B T_M} + e^{-\Delta E_P/k_B T_M}} \quad (4)$$

where $T_M = (T_1 + T_2)/2 = T_1 + \Delta T/2$ is the average temperature of the system. From Eq. (38) it can be readily seen that the requirement for kinetic selection, i.e. scenarios where one of the barriers is appreciably higher than the average temperature and the other lower, correspond to the timescale-matching condition $\text{Da}^* = \mathcal{O}(1)$ when the fast reaction is regulated by an energy barrier of roughly the same order as the average temperature.

The rationale behind non-equilibrium stabilisation of furanose becomes obvious once

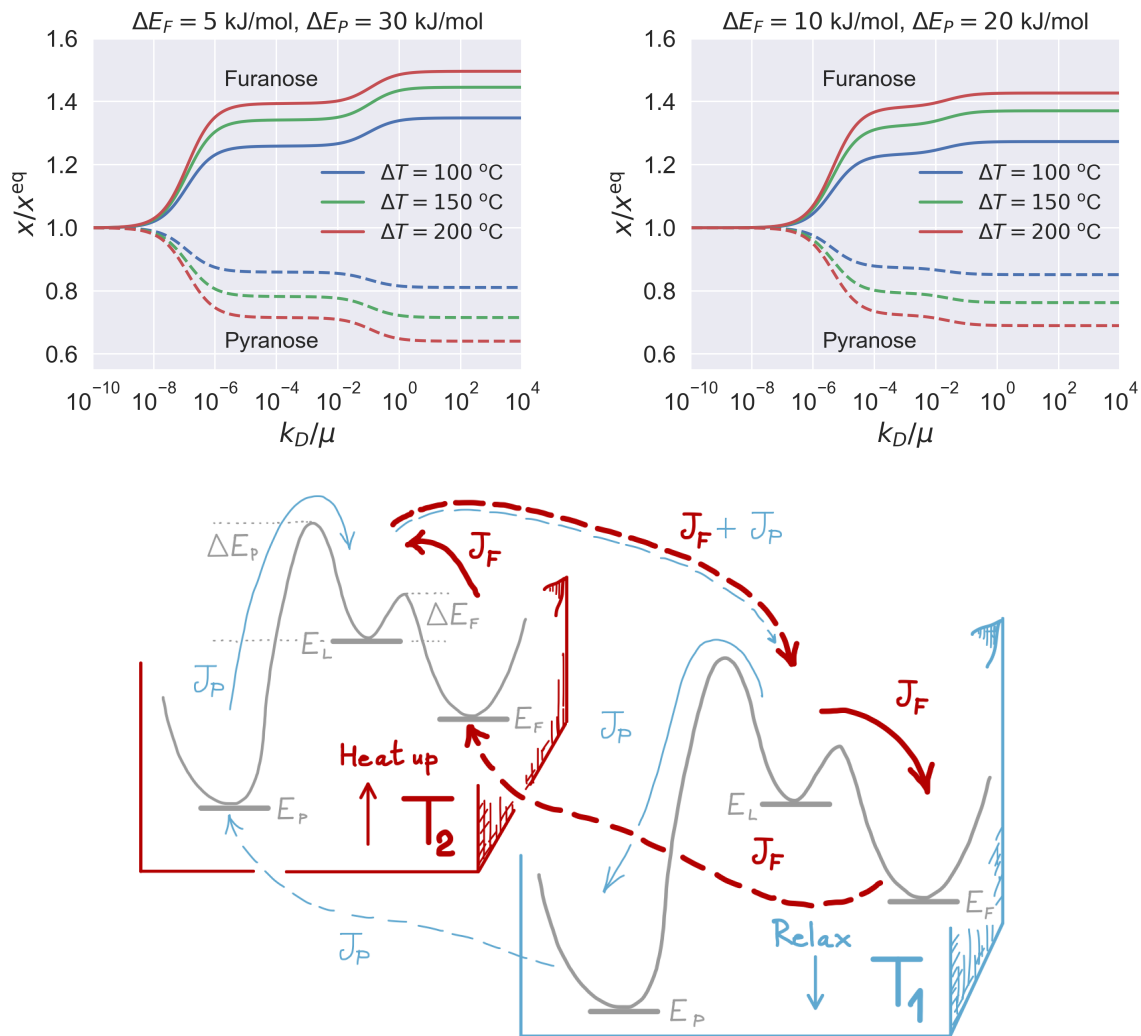


Figure 4: **Top.** Increasing the transport rate for $\Delta E_F < \Delta E_P$ leads to nonequilibrium kinetic selection of furanose beyond thermodynamic equilibrium. The steady-state molar fractions of furanose (solid lines) and pyranose (dashed lines) computed for the two-box model illustrated in Fig. 7 are plotted against the transport rate for different choices of the temperature gradient $\Delta T = T_2 - T_1$ and two choices of energy barriers (see Supplementary Material for the mathematical details). Populations are normalised to the equilibrium values, i.e. $x^{\text{eq}} \equiv (x_F^{\text{eq}}(T_1) + x_F^{\text{eq}}(T_2))/2$. **Bottom.** The energy harvested at the hot end is dissipated at the cold end, thus causing population inversion. Illustration of the steady system of currents that sustain the non-equilibrium stabilisation of furanose for $\Delta E_P > \Delta E_F$. Dashed arrows denote mass transport, solid lines stand for chemical transformations. The current J_P is much smaller than J_F in the fast transport limit, $\text{Da} \lesssim 1$. Parameters used in the two-box model are: $T_1 = 60 \text{ }^\circ\text{C}$, $\eta_F = 29.34$, $\eta_P = 1.94$, $E_L = 19 \text{ kJ/mol}$, $E_F = 13.6 \text{ kJ/mol}$, $E_P = 3.1 \text{ kJ/mol}$, corresponding to the average values for the two furanose and pyranose enantiomers measured from our equilibrium NMR experiments (see Table 1).

the system of steady fluxes is examined in detail, as illustrated in Fig. 4, bottom (see also Supplementary material). When $E_L \rightarrow E_P$ relaxation is the faster pathway out of the transition state, the furanose population is boosted by a large sustained mass current that supplies high-energy linear molecules from the hot end that undergo ring-closure at the cold side (thick red arrows). A much smaller current circulates in the same direction (thin blue arrows), weakly contributing to the steady mass current of linear D-ribose with pyranose molecules that open up at the hot end.

To summarise, when time scales for transport and chemical transformations match, part of the energy supplied by the temperature gradient can be converted into chemical energy through cycles involving mass transport. Thus, non-equilibrium population inversion may occur if the fastest reaction is fast enough, as gauged by the relative magnitude of ΔE_P and ΔE_F (see again Fig. 4). The physical consequences of this non-equilibrium phenomenon cannot be stressed enough. It is sufficient to note, for example, that the thermal energy provided by a steady gradient of $\Delta T = 100^\circ\text{C}$ between $T_1 = 60^\circ\text{C}$ and $T_2 = 160^\circ\text{C}$ is enough to boost the population of furanose to about 50 %. By contrast, when the same energy $k_B\Delta T$ is provided at thermal equilibrium, the total molar fraction of furanose is only 34 %. The extent of this non-equilibrium effect is illustrated in Table 2, where the temperature needed to obtain a given molar fraction of furanose at equilibrium is compared to the gradient required to obtain the same value in a non-equilibrium steady state. It can be clearly appreciated that the population boost obtained in a non-equilibrium setting outperforms by far the stabilisation achievable at equilibrium, allowing for molar fractions of furanose that could only be produced at exceedingly high temperatures in thermal equilibrium.

Table 2: Temperature T^* required to obtain a given overall molar fraction of furanose, x_F , at equilibrium, compared to different choices of gradients that yield the same populations in a non-equilibrium steady state. Two choices of energy barriers are considered. Note that non-equilibrium stabilisation of furanose is more effective in all cases considered, according to the stringent criterion $T^* > T_2$. All temperatures are expressed in °C.

T_1	T_2	ΔT	$\Delta E_F = 5 \text{ kJ/mol}$		$\Delta E_F = 5 \text{ kJ/mol}$	
			$\Delta E_P = 30 \text{ kJ/mol}$		$\Delta E_P = 20 \text{ kJ/mol}$	
			x_F	T^*	x_F	T^*
60	160	100	0.47	174	0.46	168
60	210	150	0.56	241	0.55	234
60	260	200	0.62	301	0.61	290

Nonequilibrium selection of furanose is maximum at optimal dissipation

The simple two-box model discussed in the preceding section can be easily generalised in the continuum limit to a system of reaction-diffusion partial differential equations. For the sake of simplicity, and with no loss of generality, we shall restrict ourselves to a one-dimensional system. Let the reactants be confined to a one-dimensional box of length L with reflecting boundary conditions at $x = 0$ and $x = L$ and let $T(x)$ indicate the imposed temperature gradient across the box, or any arbitrary temperature profile with the same boundary conditions, $T(0) = T_1, T(L) = T_2$. We define the space- and time-dependent chemical molar fractions, $\mathcal{P}_\sigma(x, t)$, $\sigma = F, P, L$. The equations then read

$$\begin{aligned}
 \frac{\partial \mathcal{P}_F(x, t)}{\partial t} &= D \frac{\partial^2 \mathcal{P}_F(x, t)}{\partial x^2} + k_{LF}(x) \mathcal{P}_L(x, t) - k_{FL}(x) \mathcal{P}_F(x, t) \\
 \frac{\partial \mathcal{P}_P(x, t)}{\partial t} &= D \frac{\partial^2 \mathcal{P}_P(x, t)}{\partial x^2} + k_{LP}(x) \mathcal{P}_L(x, t) - k_{PL}(x) \mathcal{P}_P(x, t) \\
 \frac{\partial \mathcal{P}_L(x, t)}{\partial t} &= D \frac{\partial^2 \mathcal{P}_L(x, t)}{\partial x^2} + k_{FL}(x) \mathcal{P}_F(x, t) + k_{PL}(x) \mathcal{P}_P(x, t) + \\
 &\quad - (k_{LF}(x) + k_{LP}(x)) \mathcal{P}_L(x, t)
 \end{aligned} \tag{5}$$

where D is the diffusion coefficient (assumed to be the same for all species) and the rates are given by the obvious generalisations of the expressions introduced in the two-box model (see again Fig. 7), that is,

$$\begin{aligned} k_{FL}(x) &= \frac{\mu}{\eta_F} e^{-(E_L - E_F + \Delta E_F)/k_B T(x)} & k_{LF}(x) &= \mu e^{-\Delta E_F/k_B T(x)} \\ k_{PL}(x) &= \frac{\mu}{\eta_P} e^{-(E_L - E_P + \Delta E_P)/k_B T(x)} & k_{LP}(x) &= \mu e^{-\Delta E_P/k_B T(x)} \end{aligned} \quad (6)$$

The steady-state populations, $\mathcal{P}_\sigma^\infty(x) = \lim_{t \rightarrow \infty} \mathcal{P}_\sigma(x, t)$, are the solutions of the system obtained by letting the time derivatives vanish in Eqs. (6), with the normalisation $\mathcal{P}_F^\infty(x) + \mathcal{P}_P^\infty(x) + \mathcal{P}_L^\infty(x) = 1$ (the stationary profiles are nearly flat). In the presence of a temperature gradient, a selection indicator can be defined to quantify the excess fraction of furanose, namely

$$\mathcal{R}_{\text{sel}} = \frac{\int_0^L \mathcal{P}_F^\infty(x) dx \int_0^L \mathcal{P}_P^{\text{eq}}(x) dx}{\int_0^L \mathcal{P}_P^\infty(x) dx \int_0^L \mathcal{P}_F^{\text{eq}}(x) dx} \quad (7)$$

where $\mathcal{P}_\sigma^{\text{eq}}(x) = \eta_\sigma \exp[-E_\sigma/k_B T(x)]/Z$ stands for the equilibrium distributions. By definition, for $T(x) = \text{const.}$, the selection indicator (7) is unity.

The plots reported in Fig. 5 not only confirm the results obtained within the two-box model, but also reveal a remarkable fact. Nonequilibrium selection of furanose typically displays a maximum enhancement, corresponding to a restricted region of values of the temperature gradient $\Delta T = T_2 - T_1$ and energy barrier ΔE_F . The maximum appears to correspond to a population boost of 40 – 50 %, for a wide range of transport regimes (as gauged by the Damköhler number) and kinetic parameters, notably the values of the barrier ΔE_P . It can be appreciated that in the infinite-transport limit, $\text{Da} < 1$, the optimum is progressively pushed to lower values of the energy barrier ΔE_F . Most intriguingly, the optimal value of temperature gradient appears to be consistently not far from the gradients found in hydrothermal venting associated with extremely fresh lava flows on the seafloor, with exit temperatures up to 407 °C recorded.³⁸ It appears therefore possible that optimal

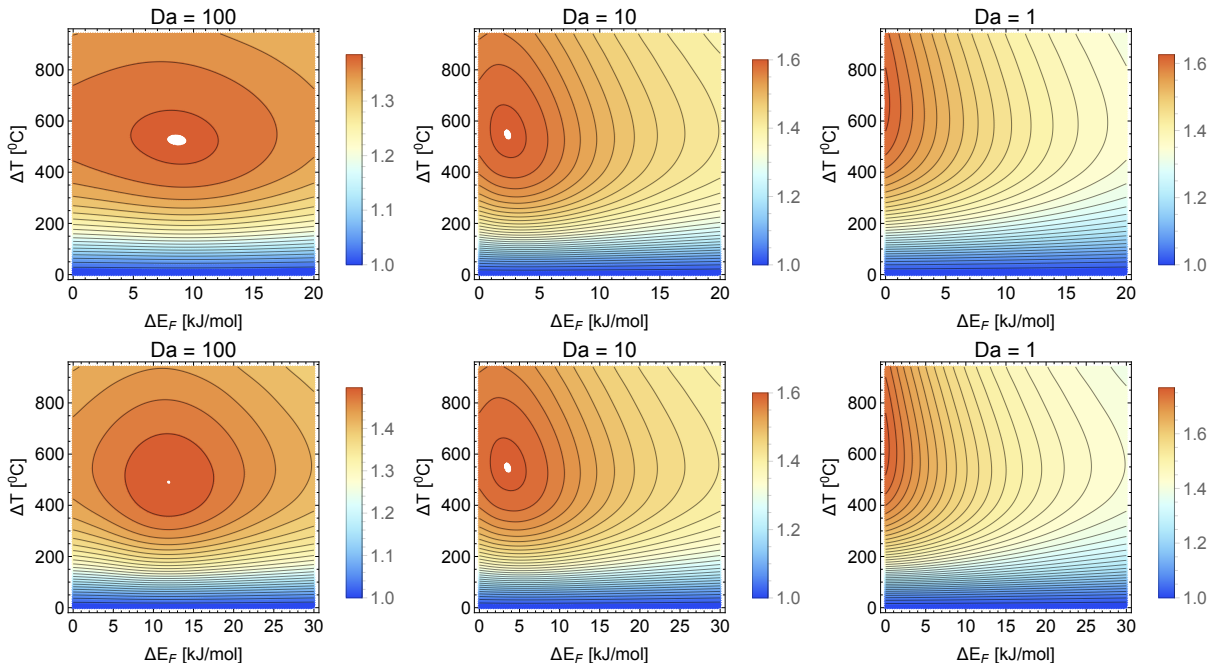


Figure 5: **Furanose selection is maximum for specific values of the temperature gradient depending on kinetic parameters.** Density plots of the normalised selection indicator \mathcal{R}_{sel} , Eq. (7), in the $(\Delta T, \Delta E_F)$ plane computed from the steady-state solutions of the continuum model (5) for different values of the Damköhler number $Da = \mu/DL^2$. The temperature profile is $T(x) = T_1 + \Delta T x/L$. Top panels: $\Delta E_P = 20$ kJ/mol. Bottom panels: $\Delta E_P = 30$ kJ/mol. Other parameters as in Fig. 4.

or suboptimal conditions could have been met at certain spots on the bottom of Hadean oceans.

Summary and discussion

In this paper we have delved into the question of why the β -furanose isoform of D-ribose has been selected as the exclusive sugar component of nucleic acids instead of pyranose, despite being far more unstable and hence present at lower molar fractions in thermodynamic equilibrium up to relatively high temperatures. Our findings suggest that a plausible answer to this question is non-equilibrium enrichment beyond equilibrium sustained by a temperature gradient.

In the first part of this work, we analyse the results of NMR measurements of ribose

isomerisation at equilibrium at increasing temperatures. A simple thermodynamic equilibrium model reproduces the NMR data to an excellent extent, revealing that the populations of the more unstable furanose species increase with temperature, while those of pyranoses decrease. As a result, a population inversion to a furanose-rich phase is predicted to occur at a temperature of about 150 °C, directly connected to the large entropic degeneracy associated with furanose internal isoforms. Remarkably, the same measurements repeated in the presence of a salt mixture simulating that of Hadean oceans led to an inversion temperature about 20 °C lower.

While high temperatures must have been ubiquitous in the early-earth environment, , at least close to the rock/water interface, it is highly unlikely that the kind of hotbeds suggested as possible primeval chemical reactors were at thermodynamic equilibrium. Building on this idea, and on the physical parameters measured in our NMR experiments, in the second part of the paper we pursue the idea that furanose might have been stabilised beyond the limits imposed by equilibrium thermodynamics under non-equilibrium conditions. To this end, we investigate a simple model of ribose isomerisation in the presence of a steady temperature gradient. Our calculations show that driving the network far from equilibrium may lead to sustained *kinetic selection* of furanose, i.e. increased stabilisation with respect to thermal equilibrium, if linear-to-furanose interconversion proceeds appreciably faster than linear-to-pyranose.

The increased stabilisation occurs as diffusive and convective mass currents set in, shuttling molecules cyclically across the temperature gradient. Thus, in the non-equilibrium steady state, sustained mass transport and chemical transformations may couple in such a way that furanose molecules absorb heat at the hot side and are transported to the cold end, where the extra heat is used to steer chemical relaxation towards the production of more furanose. We show that this scenario may emerge provided (i) the typical Damköhler number of the system is of lower than about 1 – 10 (depending on energy barriers), and (ii) the relaxation of linear ribose to furanose is faster than its relaxation to pyranose. Ac-

ording to the first requirement, timescales characteristic of mass transport should roughly match those typical of chemical transformations. If this is the case, the fastest reactions will be kinetically selected, and the populations of associated products boosted beyond thermal equilibrium through sustained mass currents. The second requirement, amounts to a condition on the relative magnitude of the energy barriers that separate chemical states in the system. While these are strictly irrelevant at equilibrium, in systems driven away from equilibrium, (kinetic) selection of the fittest may be achieved as selection of the fastest.

Variations of the temperature gradient and energy barriers have a profound effect on the extent of furanose nonequilibrium selection. We show that ultra-stabilisation is maximum in specific regions of parameter space. Intriguingly, optimal temperature gradients are predicted in the range 300 – 400 °C, of the same order of magnitude as those found in the proximity of present-day venting activity at some spots on the seafloor.³⁸ This prompts the intriguing hypothesis that *kinetic landscapes* such as those illustrated in Fig. 5 might have been integrated by evolution in more comprehensive, multi-fitness landscapes that eventually led to the biochemistry of life that we know today.

In summary, an accurate thermodynamic characterisation of ribose isomerisation revealed the occurrence of population inversion between furanose and pyranose species at increasing temperatures in thermal equilibrium. However, we demonstrated that the constraints imposed by equilibrium thermodynamics can be overcome and more furanose produced by driving the network far from equilibrium through a steady temperature gradient.

Acknowledgements

AVD and FW would like to acknowledge Region Centre, France, for a doctoral bursary for AVD.

References

- (1) Gilbert, W. Origin of life: The RNA world. *Nature* **1986**, *319*, 618.
- (2) Butlerow, A. Bildung einer zuckerartigen Substanz durch Synthese. *Justus Liebigs Annalen der Chemie* **1861**, *120*, 295–298.
- (3) Breslow, R. On the mechanism of the formose reaction. *Tetrahedron Letters* **1959**, *1*, 22–26.
- (4) Orgel, L. E. Self-organizing biochemical cycles. *Proceedings of the American Philosophical Society* **2000**, *97*, 12503–12507.
- (5) Decker, P.; Schweer, H.; Pohlmann, R. Identification of formose sugars, presumable prebiotic metabolites, using capillary gas chromatography/gas chromatography-mass spectrometry of n-butoxime trifluoroacetates on OV-225. *Journal of Chromatography* **1982**, *244*, 281–291.
- (6) Larralde, R.; Robertson, M. P.; Miller, S. L. Rates of decomposition of ribose and other sugars: Implications for chemical evolution. *Proceedings of the National Academy of Sciences of the United States of America* **1995**, *92*, 8158–8160.
- (7) Georgelin, T.; Jaber, M.; Fournier, F.; Laurent, G.; Costa-Torro, F.; Maurel, M.-C.; Lambert, J.-F. Stabilization of ribofuranose by a mineral surface. *Carbohydrate Research* **2015**, *402*, 241–244.
- (8) Drew, K. N.; Zajicek, J.; Bondo, G.; Bose, B.; Serianni, A. S. ¹³C-labeled aldopentoses: detection and quantitation of cyclic and acyclic forms by heteronuclear 1D and 2D NMR spectroscopy. *Carbohydrate Research* **1998**, *307*, 199–209.
- (9) Singh, P.; Singh, A.; Kaur, J.; Holzer, W. H-Bond activated glycosylation of nucleobases: Implications for prebiotic nucleoside synthesis. *RSC Advances* **2014**, *4*, 3158–3161.

- (10) Kolb, V. M.; Zhu, W. Complexes of ribose with silicates, borates, and calcium: Implications to Astrobiology. Instruments, Methods, and Missions for Astrobiology VIII. Bellingham, WA, 2004, 2004; pp 70–77.
- (11) Benner, S. A.; Kim, H.-J.; Kim, M.-J.; Ricardo, A. Planetary Organic Chemistry and the Origins of Biomolecules. *Cold Spring Harbor Perspectives in Biology* **2010**, *2*, a003467, pp.21.
- (12) Lambert, J. B.; Lu, G.; Singer, S. R.; Kolb, V. M. Silicate complexes of sugars in aqueous solution. *Journal of the American Chemical Society* **2004**, *126*, 9611–9625.
- (13) Westall, F.; Hickman-Lewis, K.; Hinman, N.; Gautret, P.; Campbell, K.; Bréhéret, J.; Foucher, F.; Hubert, A.; Sorieul, S.; Dass, A.; Kee, T.; Georgelin, T.; Brack, A. A Hydrothermal-Sedimentary Context for the Origin of Life. *Astrobiology* **2018**, *18*, 259–293.
- (14) Tartèse, R.; Chaussidon, M.; Gurenko, A.; Delarue, F.; Robert, F. Warm Archean oceans reconstructed from oxygen isotope composition of early-life remnants. *Geochemical Perspectives Letters* **2017**, *3*, 55–65.
- (15) Smith, E.; Morowitz, H. J. *The Origin and Nature of Life on Earth*; Cambridge University Press, 2016.
- (16) Möller, F. M.; Kriegel, F.; Kieß, M.; Sojo, V.; Braun, D. Steep pH Gradients and Directed Colloid Transport in a Microfluidic Alkaline Hydrothermal Pore. *Angewandte Chemie - International Edition* **2017**, *56*, 2340–2344.
- (17) Mast, C. B.; Schink, S.; Gerland, U.; Braun, D. Escalation of polymerization in a thermal gradient. *Proceedings of the National Academy of Sciences of the United States of America* **2013**, *110*, 8030–8035.

- (18) Agerschou, E. D.; Mast, C. B.; Braun, D. Emergence of Life from Trapped Nucleotides? Non-Equilibrium Behavior of Oligonucleotides in Thermal Gradients. *Synlett* **2017**, *28*, 56–63.
- (19) Lane, N. Proton gradients at the origin of life. *BioEssays* **2017**, *39*.
- (20) Morasch, M.; Braun, D.; Mast, C. B. Heat-Flow-Driven Oligonucleotide Gelation Separates Single-Base Differences. *Angewandte Chemie - International Edition* **2016**, *55*, 6676–6679.
- (21) Rao, R.; Esposito, M. Nonequilibrium thermodynamics of chemical reaction networks: Wisdom from stochastic thermodynamics. *Physical Review X* **2016**, *6*, 041064.
- (22) Nicolis, G.; Prigogine, I. *Self-organization in nonequilibrium systems*; John Wiley & Sons: New York, NY, 1977.
- (23) Stich, M.; Ribó, J. M.; Blackmond, D. G.; Hochberg, D. Necessary conditions for the emergence of homochirality via autocatalytic self-replication. *The Journal of Chemical Physics* **2016**, *145*, 074111.
- (24) Ge, H.; Qian, M.; Qian, H. Stochastic theory of nonequilibrium steady states. Part II: Applications in chemical biophysics. *Physics Reports* **2012**, *510*, 87–118.
- (25) Pross, A. The driving force for life’s emergence: Kinetic and thermodynamic considerations. *Journal of Theoretical Biology* **2003**, *220*, 393–406.
- (26) Busiello, D. M.; Liang, S.-L.; Piazza, F.; De Los Rios, P. Dissipation-driven selection in non-equilibrium chemical networks. **2019**, arXiv:1912.04642.
- (27) Roduner, E.; Radhakrishnan, S. G. In command of non-equilibrium. *Chem Soc Rev* **2016**, *45*, 2768–2784.
- (1) Dass, A. V. Stochastic Prebiotic Chemistry. Ph.D. thesis, Health, Biological Sciences and Chemistry of Life (SSBCV), 2018.

- (29) Cocinero, E. J.; Lesarri, A.; Écija, P.; Basterretxea, F. J.; Grabow, J. U.; Fernández, J. A.; Castaño, F. Ribose found in the gas phase. *Angewandte Chemie - International Edition* **2012**, *51*, 3119–3124.
- (30) Barge, L. M.; Flores, E.; Baum, M. M.; VanderVelde, D. G.; Russell, M. J. Redox and pH gradients drive amino acid synthesis in iron oxyhydroxide mineral systems. *Proceedings of the National Academy of Sciences of the United States of America* **2019**, *116*, 4828–4833.
- (31) Sojo, V.; Herschy, B.; Whicher, A.; Camprubí, E.; Lane, N. The Origin of Life in Alkaline Hydrothermal Vents. *Astrobiology* **2016**, *16*, 181–197.
- (32) Spitzer, J. Emergence of Life from Multicomponent Mixtures of Chemicals: The Case for Experiments with Cycling Physicochemical Gradients. *Astrobiology* **2013**, *13*, 404–413.
- (33) Cockell, C. S. The origin and emergence of life under impact bombardment. *Philosophical Transactions of the Royal Society B: Biological Sciences* **2006**, *361*, 1845–1855.
- (34) Endres, R. G. Entropy production selects nonequilibrium states in multistable systems. *Scientific Reports* **2017**, *7*, 14437.
- (35) England, J. L. Dissipative adaptation in driven self-assembly. *Nature Nanotechnology* **2015**, *10*, 919–923.
- (36) Meysman, F. J.; Bruers, S. Ecosystem functioning and maximum entropy production: A quantitative test of hypotheses. *Philosophical Transactions of the Royal Society B: Biological Sciences* **2010**, *365*, 1405–1416.
- (37) Göppel, T.; Palyulin, V. V.; Gerland, U. The efficiency of driving chemical reactions by a physical non-equilibrium is kinetically controlled. *Physical Chemistry Chemical Physics* **2016**, *18*, 20135–20143.

- (38) Haase, K. M. et al. Young volcanism and related hydrothermal activity at 5 °S on the slow-spreading southern Mid-Atlantic Ridge. *Geochemistry, Geophysics, Geosystems* **2007**, *8*.

Supplementary material

NMR experiments

Choice of the relaxation time T_1 in the NMR experiments

The first step in order to quantify the relative population of each anomer through ^{13}C NMR experiments is to evaluate the relaxation time T_1 for all species. Since T_1 is strongly dependent on temperature, T_1 measurements were carried out at each temperature before the spectral data were recorded. The results of these experiments are reported in Table 3. It can be appreciated that T_1 increases significantly with temperature from about 2 to 5

Table 3: Values of T_1 (seconds) for C1 of ribose at thermal equilibrium at different temperatures.

Temperature ($^{\circ}\text{C}$)	αP	αF	βP	βF
20	1.99	1.59	1.79	1.87
30	2.37	2.85	2.42	2.15
40	2.74	3.62	2.77	2.91
50	3.77	3.56	3.51	3.74
60	5.06	5.49	5.19	5.10
70	5.79	6.44	5.11	5.18
80	7.94	5.16	6.11	5.79

seconds, for temperatures between 10 $^{\circ}\text{C}$ and 80 $^{\circ}\text{C}$, the temperature range of this study. Overall, however, it is fair to say that the values of T_1 are similar for all anomers at a given temperature. Only α pyranose shows a significantly higher value at the higher temperature of 80 $^{\circ}\text{C}$. Building on these results, we investigated the anomerisation of ribose by ^{13}C NMR at different temperatures, by adapting the D_1 ($5T_1$) for each experiment.

Extracting the equilibrium molar fractions from the NMR spectra

At 25 $^{\circ}\text{C}$ ($T_1 = 1.8$ s), the signals of C1- αP , C1- βP , C1- αF and C1- βF are found, respectively, at 93.56 ppm, 93.85 ppm 96.33 ppm and 100.99 ppm. A large number of ^{13}C NMR

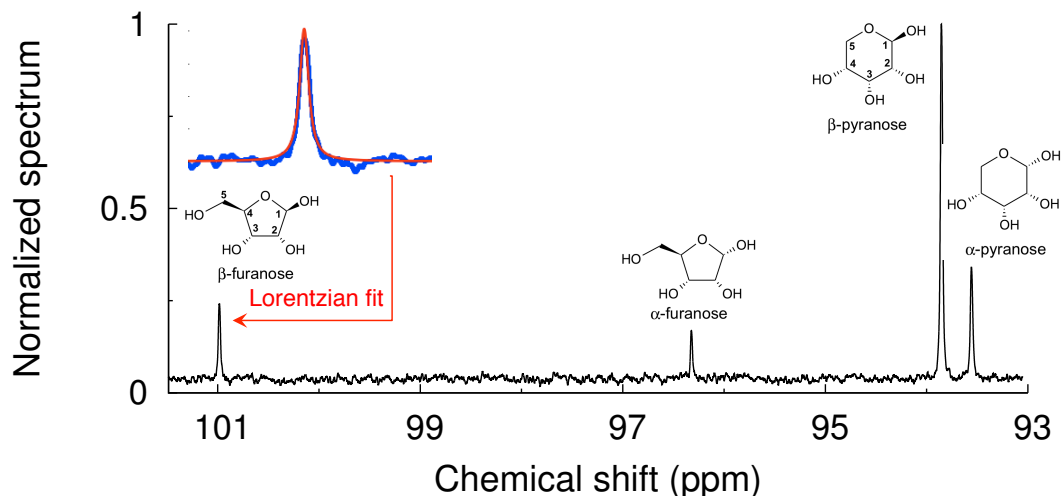


Figure 6: ^{13}C NMR spectrum of D-ribose in solution at $T = 25\text{ }^\circ\text{C}$ and ambient pressure. The relative fractions of the four species x_i were estimated by fitting the areas A_i below the respective NMR peaks, i.e. $x_i = A_i / \sum_m A_m$. The inset shows a typical Lorentzian fit of one of the anomers' peak.

spectra, between 50 and 80, was recorded for each temperature and the average relative molar fractions computed by fitting the corresponding peak areas with Lorentzian line shapes. This procedure is illustrated for one representative spectrum in Fig. 6.

Model Hadean water

The composition of the artificial sea water¹ used in our NMR experiments is reported in Table 4.

Table 4: Salt composition of the simulated Hadean sea water used in our ^{13}C NMR experiments, pH 6.3.

Compound	g/L
NaCl	70.00
NaSiO ₂	0.30
FeCl ₂	0.30
KCl	1.40
NaHCO ₃	0.10
KBr	0.30
H ₃ BO ₃	0.20
NaF	0.50
MgCl ₂ · 6H ₂ O	19.30

- NaCl in the modern ocean is 35g/L, and has maximum values at the vents of hydrothermal systems. Fluid inclusion study demonstrates that the concentration of NaCl exceeds current levels in both Archaean seawater and hydrothermal fluid. Zharkov² supported an Archaean sea of 1.2 times the current salinity, inferring lacking complexity of biological evolution. This was refuted by Knauth,³ who advocated an ocean at least 1.6 times as saline as the modern. de Ronde et al.⁴ conducted detailed fluid inclusion studies in Barberton Greenstone Belt ironstones to assign ionic concentrations to the water in which those formed. We have selected the hydrothermal end-member of their dataset as being the example which most closely represents the environment we aim to simulate. Therefore, the Archaean ocean at the sediment-hydrothermal water interface is approximately twice the salinity of the modern ocean, 70 g/L. Rollinson⁵ suggests that the Archaean ocean was saturated in both the ions of Na and Cl.
- NaSiO₂ is added to provide the Si ion. The continued addition of Na is inconsequential, as explained above it was oversaturated. Knauth⁶ suggests that in an ocean of 50 °C, Si would have a concentration of 300ppm, however, Rimstidt⁷ had previously given a conservative estimate of only 20ppm. Early Archaean stratigraphy is profoundly and ubiquitously silicified throughout, particularly in the hydrothermally influenced shallow water environments which we aim to simulate in this experiment. Therefore, we chose the value of 300ppm (0.3 g/L), with the observation that this is perhaps even a conservative estimate of the waters. Knauth's estimation was for the whole ocean; unfortunately, the modern hydrothermal analogues are not strictly equivalent to ancient examples.
- FeCl₂ was chosen to replace the FeSO₄ of the modern ocean, and is specifically to add Fe; as mentioned above, the saturation of the ocean in Cl⁵ means that its overaddition should not affect our estimation. SO₄ was low to negligible in the Hadean-Archaean ocean,^{8,9} but there was a substantial Fe dissolved reservoir;^{10,11} Fe in Archaean car-

bonate indicates that concentrations in the equilibrating ocean were twice their current values. We consider the example of Lac Pavin, France, a supposed Archaean analogue water body featuring an iron system.¹² Throughout the lake profile, Fe concentrations vary from 2 μM in the top waters to 2,400 μM in the iron-rich waters at the base; we select the latter value as representative of the hydrothermal scenario that we propose. This value is similar to those of Archaean and modern hydrothermal zone Fe concentration described by Douville et al.¹³⁻¹⁵ It exceeds the 40-120 μM suggested by Canfield,^{10,16,17} though their estimations represent oceanic concentrations, which we consider to be the seawater end-member.

- KCl is added to provide the K ion, which would have been sourced from effusions of hydrothermal fluids and dissolution of feldspar. Rollinson⁵ suggests that K concentration was 19 mM in the Archaean ocean. We consider that this estimate may be conservative, however, there would have been a limited flux from erosion of the seafloor which, being komatiite-basalt in composition, has low, but not negligible, K content.
- NaHCO_3 provides the bicarbonate, and Na, which was saturated. Using the relationships of dissolved carbonates in the ocean, we conclude that at pH 6, 70 % (0.7 mole fraction) of total carbonate would have been bicarbonate. Thus, of the three phases in the carbonate diagram, bicarbonate would be the dominant phase. The presence of carbonates in the Archaean is understood only poorly due to a paucity in their preservation. We have used the pre-industrial value of bicarbonate, 1, 757 $\mu\text{M}/\text{L}$, to ensure that the ion is present, though this is the least well-constrained component.
- KBr is added for the Br ion which, from fluid inclusion studies of 3.23 Ga ironstone pods in Barberton, is estimated at 2.59 mM/L for the hydrothermal end-member. A corollary of this addition is the addition of K, which has already been accounted for in KBr.
- H_3BO_3 is chosen for the BO_3 ion. Modern values are 4-5 ppm (0.005 g/L), which we

take as the absolute minimum for Archaean values. Since borate is associated with hydrothermal activity, we have taken the values of current hydrothermal fluids at 203 °C as indicative of the levels of borate present in our simulated hydrothermal scenario. Therefore, 0.2 g/kg of the compound is needed.¹⁸

- NaF is added for the F ion, which is major in hydrothermal effusions. No data for F was extracted from the ironstone fluid inclusions of de Ronde et al.,⁴ no from any other example in our extensive literature survey. We thus turned to modern submarine hydrothermal systems as the closest available analogue. Values include 44 $\mu\text{M}/\text{L}$, 36.2-65.4 μM (of which the 40.2-42.9 μM bracket (cool flange) may be most representative: island arc hydrothermal field, and 500 ppm in an ore-forming fluid (since this fluid is an ore-forming example, the value is likely a slight overestimation of our more passive hydrothermal scenario).
- $\text{MgCl}_2 \cdot 6\text{H}_2\text{O}$ is added for Mg, and since the ultramafic oceanic crust was rich in olivine-containing rocks (komatiite and tholeiite), we have taken the upper limit estimated by Rollinson⁵ of 95 mM/L.
- $\text{CaCl}_2 \cdot 2\text{H}_2\text{O}$ is added for Ca, and since pyroxene was a major mineral in the reactive (dissolution of volcanic glass and feldspar) ultramafic oceanic crust, we have taken the upper limit estimate by Rollinson⁵ of 50 mM/L.

Theory

In the following, the energy of furanose (F) is referred to as E_1 , that of pyranose (P) as E_2 , while that of the transition state, linear sugar (L) is referred to as E_0 .

Diagrammatic calculation of the steady-state molar fractions

With reference to the node numbering shown in Fig. 7, the rate equations associated with the reduced reaction network (one high-energy (F) state E_1 , one low-energy (P) state E_2 and a transition state, E_0) read

$$\begin{aligned}
 \dot{x}_0 &= k_{10}x_1 + k_{50}x_5 + k_Dx_3 - (k_{01} + k_{05} + k_D)x_0 \\
 \dot{x}_1 &= k_{01}x_0 + k_Dx_2 - (k_{10} + k_D)x_1 \\
 \dot{x}_2 &= k_{32}x_3 + k_Dx_1 - (k_{23} + k_D)x_2 \\
 \dot{x}_3 &= k_{23}x_2 + k_{43}x_4 + k_Dx_0 - (k_{32} + k_{34} + k_D)x_3 \\
 \dot{x}_4 &= k_{34}x_3 + k_Dx_5 - (k_{43} + k_D)x_4 \\
 \dot{x}_5 &= k_{05}x_0 + k_Dx_4 - (k_{50} + k_D)x_5
 \end{aligned} \tag{8}$$

with the normalisation $\sum_{m=0}^5 x_m = 1$. The explicit expressions for the rates read (see also main text):

$$\begin{aligned}
 k_{01} &= \mu e^{-\beta_2 \Delta E_1} & k_{32} &= \mu e^{-\beta_1 \Delta E_1} \\
 k_{05} &= \mu e^{-\beta_2 \Delta E_2} & k_{34} &= \mu e^{-\beta_1 \Delta E_2} \\
 k_{10} &= \frac{\mu}{\eta_1} e^{-\beta_2 (E_0 - E_1 + \Delta E_1)} & k_{23} &= \frac{\mu}{\eta_1} e^{-\beta_1 (E_0 - E_1 + \Delta E_1)} \\
 k_{50} &= \frac{\mu}{\eta_2} e^{-\beta_2 (E_0 - E_2 + \Delta E_2)} & k_{43} &= \frac{\mu}{\eta_2} e^{-\beta_1 (E_0 - E_2 + \Delta E_2)}
 \end{aligned} \tag{9}$$

where $\beta_i^{-1} = k_B T_i$, $i = 1, 2$. Following Ref. 19, the stationary state of the rate equations (8) can be computed by referring to the complete set of *partial diagrams* of the network (see

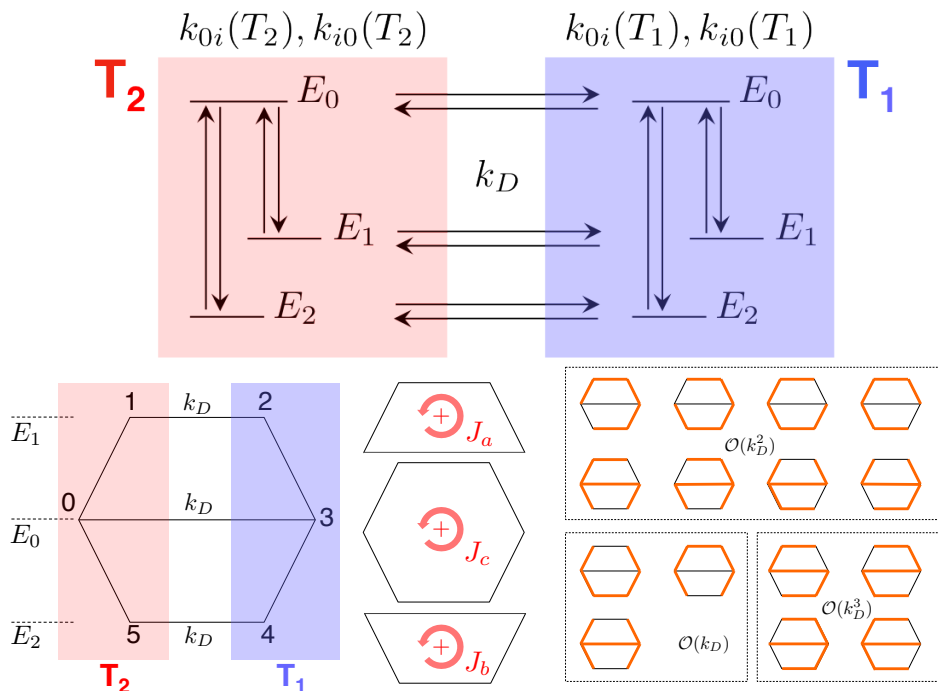


Figure 7: (Top) reduced model of ribose isomerisation reactions in a steady temperature gradient ($T_2 > T_1$). The highest-energy linear species has energy E_0 . The two furanose species have been coalesced into the high-energy species 1 (energy E_1), while the two pyranose species represent the ground state in this model. Each species can diffuse or be advected across the temperature gradient with a global rate k_D . Bottom left: Graph corresponding to the above chemical network with identification of the nodes and illustration of the three cycle fluxes present in this model. The convention for positive cycles is shown explicitly. Bottom right: the complete set of partial diagrams, each of which contains the maximum number of lines (five here) that can be included without forming a cycle. The partial diagrams are grouped according to the number of *mobility* links that they contain (i.e. branches giving a contribution proportional to k_D).

Fig. 7). The steady-state value of state m is then obtained by introducing a directionality to each line in each partial diagram, so that all connected path *flow* toward the vertex m . Each directional line corresponds to a rate constant, hence each *directional* partial diagram corresponds to the product of five rate constants. The prescription is then that each x_m is proportional to the sum of all the associated directional diagrams. It will be remarked that the partial diagrams contain either 1,2 or 3 *mobility* link, and therefore they can be classified as corresponding to terms of order k_D^n ($n = 1, 2, 3$ in the expressions for the stationary probabilities (molar fractions). As an example, considering state 1, the steady-state probability

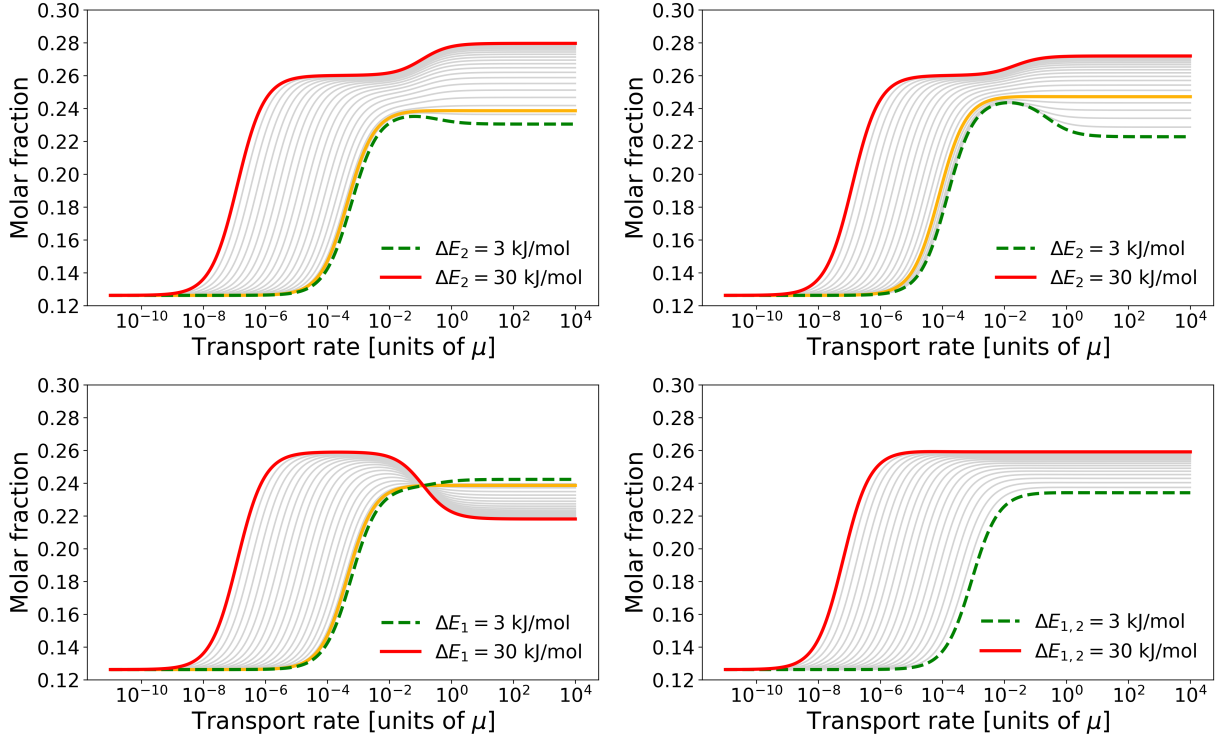


Figure 8: **Illustration of the ultra-stabilisation/ultra-destabilisation effects.** Molar fraction of the high-energy furanose species in a steady thermal gradient of the same order as that present between the top and the base of a thermal vent ($T_2 = 210\text{ }^\circ\text{C}$, $T_1 = 60\text{ }^\circ\text{C}$) as a function the transport rate k_D (in units of $\mu = k_{01}^\infty = k_{02}^\infty$) for different choices of the energy barriers $\Delta E_1, \Delta E_2$. Clockwise from top to bottom: $\Delta E_1 = 5\text{ kJ/mol}$ and varying $\Delta E_2 \in [3, 30]\text{ kJ/mol}$, $\Delta E_1 = 10\text{ kJ/mol}$ and varying $\Delta E_2 \in [3, 30]\text{ kJ/mol}$, $\Delta E_2 = 5\text{ kJ/mol}$ and varying $\Delta E_1 \in [3, 30]\text{ kJ/mol}$ (the amber lines correspond to $\Delta E_2 = \Delta E_1$), varying $\Delta E_1 = \Delta E_2 \in [3, 30]\text{ kJ/mol}$. Parameters are $\eta_1 = 29.34$, $\eta_2 = 1.945$, $E_0 = 19\text{ kJ/mol}$, $E_1 = 13.6\text{ kJ/mol}$, $E_2 = 3.1\text{ kJ/mol}$, corresponding to the average values for the two furanose and pyranose enantiomers measured from equilibrium NMR experiments (see Table I in the main text).

reads

$$x_1 = \frac{k_D^3(k_{43}k_{01} + k_{50}k_{32}) + k_D^2(k_{43}k_{32}k_{01} + [\dots]_7) + k_D(k_{50}k_{01}k_{23}k_{34} + [\dots]_2)}{k_D^3(k_{43}k_{01} + k_{50}k_{32}) + k_D^2(k_{43}k_{32}k_{01} + [\dots]_7) + k_D(k_{50}k_{01}k_{23}k_{34} + [\dots]_2) + [\dots]_{65}} \quad (10)$$

where the notation $[\dots]_n$ stands for n other terms. Overall, each expression such as eq. (10) contains 13 terms in the numerator (i.e. as many as there are partial diagrams) and 78 terms in the denominator (i.e. 13 terms multiplied 6 nodes). As stated in the main text,

such expressions can be cast in the general form of ratios of second-order polynomials, i.e.

$$x_i = \frac{\alpha_{2i}k_D^2 + \alpha_{1i}k_D + \alpha_{0i}}{A_2k_D^2 + A_1k_D + A_0}, \quad i = 0, 1, \dots, 5 \quad (11)$$

with

$$A_n = \sum_{j=0}^5 \alpha_{nj}, \quad n = 0, 1, 3 \quad (12)$$

The limit $k_D \rightarrow 0$, thermal equilibrium

In our model, the thermal equilibrium scenario corresponds to two isolated boxes, each reaching thermal equilibrium at a separate temperature. Mathematically, this corresponds to the limit $k_D \rightarrow 0$, $\text{Da} \propto k_D^{-1} \rightarrow \infty$, the steady-state populations reducing to their respective equilibrium expressions (see Eqs. (2) in the main text),

$$x_i^{\text{eq}} \stackrel{\text{def}}{=} \lim_{k_D \rightarrow 0} x_i = \frac{\alpha_{0i}}{A_0} \quad (13)$$

More precisely, we have

$$\begin{aligned} x_1^{\text{eq}} &= \frac{1}{2}P_{E_1}^{\text{eq}}(T_2) & x_2^{\text{eq}} &= \frac{1}{2}P_{E_1}^{\text{eq}}(T_1) \\ x_5^{\text{eq}} &= \frac{1}{2}P_{E_2}^{\text{eq}}(T_2) & x_4^{\text{eq}} &= \frac{1}{2}P_{E_2}^{\text{eq}}(T_1) \\ x_0^{\text{eq}} &= \frac{1}{2}P_{E_0}^{\text{eq}}(T_2) & x_3^{\text{eq}} &= \frac{1}{2}P_{E_0}^{\text{eq}}(T_1) \end{aligned} \quad (14)$$

with

$$P_{E_i}^{\text{eq}}(T) = \frac{\eta_i e^{-E_i/k_B T}}{Z(T)}, \quad (15)$$

where $Z(T) = e^{-E_0/k_B T} + \eta_1 e^{-E_1/k_B T} + \eta_2 e^{-E_2/k_B T}$ denotes the partition function at temperature T . The factor 1/2 in Eqs. (14) reflects the fact that each box contains half of the total mass.

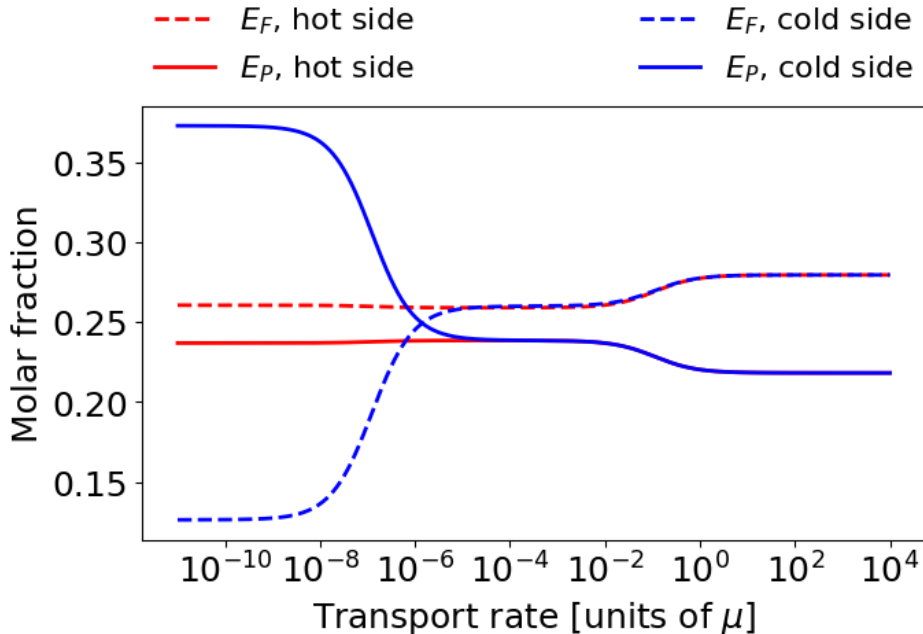


Figure 9: **The high-energy furanose species can be ultra-stabilised by sustained mass currents at large enough transport rates.** Molar fraction of furanose (dashed lines) and pyranose (solid lines) species in a steady thermal gradient with $T_2 = 210^\circ\text{C}$, $T_1 = 60^\circ\text{C}$ vs transport rate k_D in units of μ (Da^{-1}) for $\Delta E_1 = 5$ kJ/mol, $\Delta E_2 = 30$ kJ/mol. Two consecutive stabilisation crossovers are observed as the transport rate increases, the final *ultra-stabilisation* transition occurring when $\text{Da} \simeq 1$ ($k_D \simeq \mu$). Equilibrium parameters are $\eta_1 = 29.34$, $\eta_2 = 1.945$, $E_0 = 19$ kJ/mol, $E_1 = 13.6$ kJ/mol, $E_2 = 3.1$ kJ/mol, set as the average values for the two furanose and pyranose enantiomers measured from equilibrium NMR experiments (see Table I in the main text).

Finite values of the transport rate k_D , non-equilibrium steady states

As transport of reactants across the temperature gradient is put back into the picture, non-equilibrium effects start shifting the steady state away from thermal equilibrium, as sustained currents set in, coupling mass transport to chemical transformations. Fig. 9 shows clearly that, when production of furanose proceeds faster than pyranose (i.e. $\Delta E_2 > \Delta E_1$), this causes the population of furanose to grow beyond its highest equilibrium value at values of Da of order one. We refer to this non-equilibrium effect as *ultra-stabilisation* of furanose.

More precisely, with the choice of parameters derived from our NMR experiments, the steady-state solutions (11) display three regimes as a function of the transport rate k_D , identified by two distinct crossovers occurring at characteristic rates $k_D^{*[1]}$ and $k_D^{*2} \geq k_D^{*[1]}$,

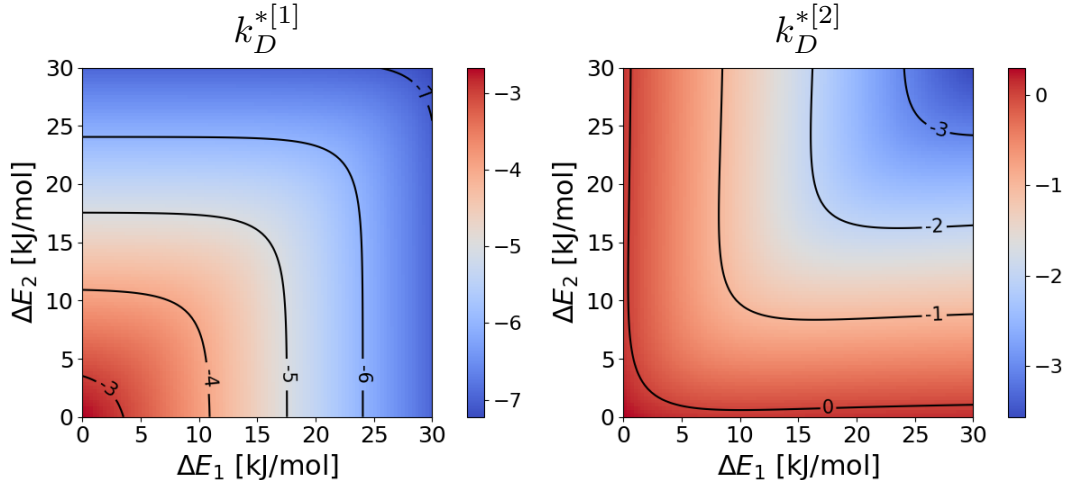


Figure 10: **The mobility rates that mark stabilisation crossovers of furanose are well separated and depend markedly on the energy barriers.** Density plot of $k_D^{*[2]}$ and $k_D^{*[1]}$ (in units of μ) in the plane $\Delta E_1, \Delta E_2$ in logarithmic (base 10) scale. Parameters as in Fig. 9 (see Table I in the main text)

as illustrated in Fig. 9. These can be computed straightforwardly from Eq. (11) and show a marked dependence on the choice of the energy barriers ΔE_1 and ΔE_2 , as illustrated by Fig. 10. However, with the choice of parameters extracted from our equilibrium experiments, it turns out that the two crossovers are always distinct, $k_D^{*[2]}$ being at least three orders of magnitude larger than $k_D^{*[1]}$ irrespective of the magnitude of the energy barriers.

Increasing k_D past $k_D^{*[1]}$, the steady-state populations of same-species states become independent of the temperature gradient. In this regime, the molar fractions at the cold side become identical to the values at the hot side and the two boxes can be regarded as a well-stirred open chemical reactor. This is due to a small, but non-zero steady mass current that circulates in the direction $0 \rightarrow 1 \rightarrow 2 \rightarrow 3 \rightarrow 4 \rightarrow 5 \rightarrow 0$ (see Fig. 7) and hence only involves transport of closed-ring species across the temperature gradient in the hot-to-cold direction. Fig. 10 (left) shows that this first non-equilibrium effect occurs in a regime where mass transport is still much slower than chemical reactions, i.e. for values of $\text{Da} = \mu/k_D > 10^3$. Our calculations show that sustained currents that stabilise the high-energy species kick in at exponentially slower transport rates as the energy barriers increase. More precisely, it can

be shown that (see the following)

$$k_D^{*[1]} \simeq \frac{\mu}{P_{E_1}^{\text{eq}}(T_1) [f_1 (e^{\Delta E_1/k_B T_1} + e^{\Delta E_2/k_B T_1}) + f_2 (e^{\Delta E_1/k_B T_2} + e^{\Delta E_2/k_B T_2})]} \quad (16)$$

where $f_i = P_{E_2}^{\text{eq}}(T_i)/P_{E_0}^{\text{eq}}(T_i)$. In other words, when the energy barriers are small, hence chemical steps faster, molecular species need to diffuse or be advected faster to settle into a different steady state than at thermal equilibrium.

When the mobility rate increases past $k_D^{*[1]}$, a second crossover to a different steady state is seen to occur at $k_D \simeq k_D^{*[2]}$. We find that, when the two energy barriers are well separated, i.e. $\Delta E_1 \ll \Delta E_2$ or $\Delta E_2 \ll \Delta E_1$, this second crossover corresponds to a Damköhler number $\text{Da}^* = \mu/k_D^{*[2]} \simeq \mathcal{O}(1)$, provided the smaller barrier does not exceed the average thermal energy provided at the hot end, $k_B T_2$. This is the fast-transport regime, where transport and chemical reaction time scales match (see Fig. 10, right). The relation between the critical value of the Damköhler number and the main determinants of relaxation kinetics, i.e. the energy barriers, can be encapsulated in a remarkably transparent formula, notably

$$\text{Da}^* = \frac{1}{e^{-\Delta E_1/k_B T_M} + e^{-\Delta E_2/k_B T_M}} \quad (17)$$

where we have indicated with $T_M = (T_1 + T_2)/2$ the average temperature of the system. From Eq. (38) it can be readily seen that the requirement for kinetic selection, i.e. scenarios where one of the barriers is much higher than the average temperature and the other much lower, indeed correspond to the timescale-matching condition $\text{Da}^* = \mathcal{O}(1)$.

The second crossover is seen to occur at the same value of Da irrespective of whether production of furanoses is faster than of pyranoses or viceversa. However, the physical consequences of this second transition turn out to be strikingly divergent, depending on which of the two barriers is the largest and on their relative magnitude. If furanose production is the fastest relaxation channel, i.e. $\Delta E_1 \ll \Delta E_2$, the second crossover leads to ultra-stabilisation

of the most unstable closed form of the sugar ², as sustained currents keep the population of furanose beyond the highest value accessible at equilibrium, $P_{E_1}^{\text{eq}}(T_2)$. It can be shown that the relative furanose-to-pyranose population takes a remarkably simple expression in the ultra-stabilisation regime

$$\frac{P_{E_1}^\infty}{P_{E_2}^\infty} \simeq \frac{P_{E_1}^{\text{eq}}(T_2)}{P_{E_2}^{\text{eq}}(T_2)} e^{(E_0 - E_1)\Delta T / k_B T_1 T_2} \quad (18)$$

where $\Delta T = T_2 - T_1$ is the temperature gradient. Eq. (18) conveys an important piece of physical information. The relative dissipation-sustained enrichment of the high-energy furanose species, E_1 , is magnified (exponentially) the larger its energy separation from the high-energy intermediate (linear) state, E_0 . Of course, the larger the temperature gradient, the greater this effect.

In general, it not difficult to check that the condition for the two-crossover trend observed in Fig. 9 to exist is

$$A_1 \gg \sqrt{A_0 A_2} \quad (19)$$

In this case, the functions x_i will display a three-plateau trend as follows

$$x_i(k_D) \simeq \begin{cases} \frac{\alpha_{0i}}{A_0} & \text{for } k_D \ll k_D^{*[1]} \\ \frac{\alpha_{1i}}{A_1} \stackrel{\text{def}}{=} x_i^{\text{int}} & \text{for } k_D^{*[1]} \ll k_D \ll k_D^{*[2]} \\ \frac{\alpha_{2i}}{A_2} & \text{for } k_D \gg k_D^{*[2]} \end{cases} \quad (20)$$

where the two crossover mobility rates are given by

$$k_D^{*[1]} = \frac{A_0}{A_1} \quad k_D^{*[2]} = \frac{A_1}{A_2} \quad (21)$$

²Conversely, if $\Delta E_1 \gg \Delta E_2$, pyranose production proceeds much faster, and it is that species which is ultra-stabilised.

With the choice of parameters extracted from our NMR experiments, the second crossover corresponds to a transport rate that is at least 3 orders of magnitude larger than that marking the first crossover (see Fig. 11).

Furthermore, with the following definitions, which mark the relevant populations that characterise the three different regimes (int for intermediate regime),

$$x_i^{\text{eq}} \stackrel{\text{def}}{=} \lim_{k_D \rightarrow 0} x_i(k_D) = \frac{\alpha_{0i}}{A_0} \quad (22)$$

$$x_i^{\text{int}} \stackrel{\text{def}}{=} \frac{\alpha_{1i}}{A_1} \quad (23)$$

$$x_i^{\infty} \stackrel{\text{def}}{=} \lim_{k_D \rightarrow \infty} x_i(k_D) = \frac{\alpha_{2i}}{A_2} \quad (24)$$

the steady-state populations, Eq. (11), can be cast in the more transparent form (see again Eq. (21))

$$x_i(k_D) = \frac{x_i^{\infty} k_D^2 + x_i^{\text{int}} k_D^{*[2]} k_D + x_i^{\text{eq}} k_D^{*[1]} k_D^{*[2]}}{k_D^2 + k_D^{*[2]} k_D + k_D^{*[1]} k_D^{*[2]}} \quad (25)$$

Analytical expressions for the two crossover rates

An analytical approximation of the crossover rates $k_D^{*[1]}$ and $k_D^{*[2]}$ can be obtained by noticing that the same crossovers are observed for the molar fractions of the same species in either box as functions of the transport rate k_D . Hence, the abscissae of the (logarithmic) inflection points can be estimated by considering ratios between same-species molar fractions.

The first crossover

In order to compute $k_D^{*[1]}$, it is expedient to focus on the high-energy species (nodes 1 and 2 in the graph, corresponding to T_2 and T_1 , respectively). We have

$$\frac{x_1}{x_2} = \frac{\alpha_{21} k_D^2 + \alpha_{11} k_D + \alpha_{01}}{\alpha_{22} k_D^2 + \alpha_{12} k_D + \alpha_{02}} \quad (26)$$

In the region of the first crossover we can neglect the terms of order k_D^2 in Eq. (26), so that

$$\frac{x_1}{x_2} \approx \frac{\alpha_{11}k_D + \alpha_{01}}{\alpha_{12}k_D + \alpha_{02}} \quad (27)$$

from which we can estimate $k_D^{*[1]}$ as

$$k_D^{*[1]} = \frac{\alpha_{02}}{\alpha_{12}} \quad (28)$$

After some algebraic manipulation, we have

$$k_D^{*[1]} = \frac{\mu}{P_{E_1}^{\text{eq}}(T_1)[Q(T_1) + Q(T_2)]} \quad (29)$$

where

$$Q(T) = \frac{P_{E_2}^{\text{eq}}(T)}{P_{E_0}^{\text{eq}}(T)} (e^{\Delta E_1/k_B T} + e^{\Delta E_2/k_B T}) \quad (30)$$

The second crossover

In this case, it is expedient to focus on the low-energy species instead (nodes 5 and 4 in the graph, corresponding to T_2 and T_1 , respectively). Thus, we have

$$\frac{x_5}{x_4} = \frac{\alpha_{25}k_D^2 + \alpha_{15}k_D + \alpha_{05}}{\alpha_{24}k_D^2 + \alpha_{14}k_D + \alpha_{04}} \quad (31)$$

In the region of the second crossover we can neglect the zero-order terms in Eq. (31), so that

$$\frac{x_1}{x_2} \approx \frac{\alpha_{25}k_D + \alpha_{15}}{\alpha_{24}k_D + \alpha_{14}} \quad (32)$$

from which we can estimate $k_D^{*[2]}$ as

$$k_D^{*[2]} = \frac{\alpha_{14}}{\alpha_{24}} \quad (33)$$

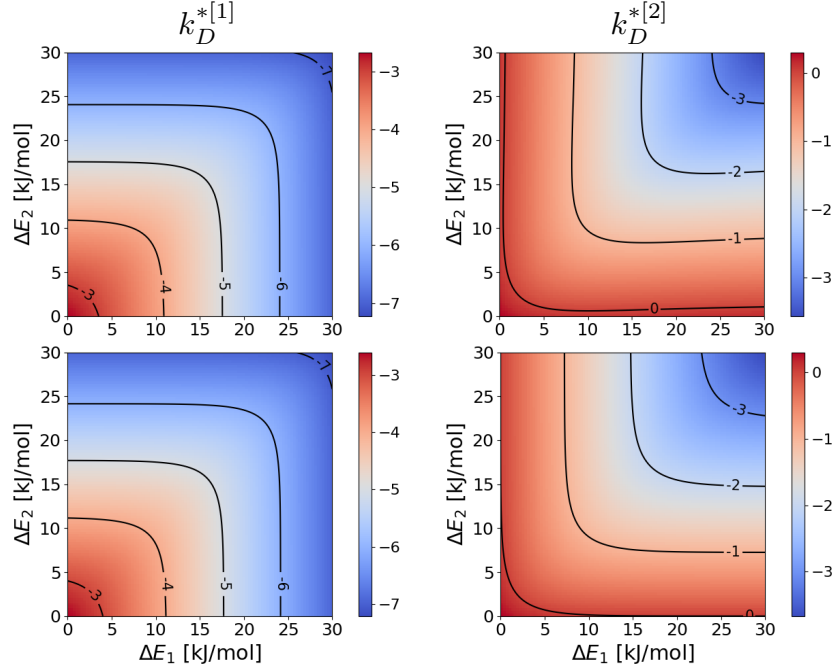


Figure 11: Density plot of $k_D^{*[2]}$ and $k_D^{*[1]}$ in the plane $\Delta E_1, \Delta E_2$ in logarithmic (base 10) scale. The top panels correspond to the exact expressions given by Eq.(21). The bottom panels are density plots of the explicit expressions, Eq. (29) ($k_D^{*[1]}$) and Eq. (38) ($k_D^{*[2]}$). Parameters are $\eta_1 = 29.34$, $\eta_2 = 1.945$, $E_0 = 19$ kJ/mol, $E_1 = 13.6$ kJ/mol, $E_2 = 3.1$ kJ/mol, corresponding to the average values for the two furanose and pyranose enantiomers measured from equilibrium NMR experiments (see main body).

The full expression in terms of the transition rates reads (see again the partial diagrams in Fig. 7)

$$k_D^{*[2]} = \frac{k_{23}k_{34}(k_{01} + k_{05}) + k_{10}k_{05}(k_{34} + k_{32}) + k_{10}k_{23}(k_{05} + k_{34}) + k_{50}k_{34}(k_{10} + k_{23})}{k_{23}k_{05} + k_{10}k_{34}} \quad (34)$$

A useful analytical expression can be derived by considering the limit $\eta_1 \rightarrow \infty$, which is seen to be a good approximation already for $\eta_1 > 0.1$. Recalling expressions (9), after some algebra, we get

$$k_D^{*[2]} = \mu \frac{G(T_1, T_2)F(T_1, T_2) + G(T_2, T_1)F(T_2, T_1)}{G(T_1, T_2) + G(T_2, T_1)} \quad (35)$$

where

$$G(T_1, T_2) = \frac{P_{E_0}^{\text{eq}}(T_1)}{P_{E_1}^{\text{eq}}(T_1)} e^{-\Delta E_1/T_1 - \Delta E_2/T_2} \quad (36)$$

$$F(T_1, T_2) = e^{-\Delta E_2/T_1} (1 + e^{(\Delta E_2 - \Delta E_1)/T_2}) \quad (37)$$

It turns out that formula (35) has an extremely simple and transparent approximation, namely

$$\begin{aligned} k_D^{*[2]} &\simeq \frac{\mu}{2} (e^{-\Delta E_1/k_B T_1} + e^{-\Delta E_2/k_B T_2} + e^{-\Delta E_2/k_B T_1} + e^{-\Delta E_1/k_B T_2}) \\ &= \mu (e^{-\Delta E_1/k_B T_M} + e^{-\Delta E_2/k_B T_M}) + \mathcal{O}(\Delta T^2) \end{aligned} \quad (38)$$

where we have indicated with $T_M = (T_1 + T_2)/2$ the average temperature of the system and with $\Delta T = T_2 - T_1$ the temperature gradient. In figure 11 we compare the explicit analytical expressions, Eq. (29) and Eq. (38), with the exact values of the crossover rates, computed through Eqs. (21). It is seen that the two analytical estimates are in excellent agreement with the results of the full calculations, including the extremely simple formula (38).

Cycle fluxes

With reference to Fig. 7, there are three cycle fluxes in our system. According to the general diagrammatic prescription described in Ref.,¹⁹ the ratio between the one-way cycle fluxes (according to the chosen convention for positive fluxes) can be computed rather straightforwardly. More precisely, one has

$$\frac{J_{a+}}{J_{a-}} = \frac{k_{32}k_{10}}{k_{23}k_{01}} = e^{(E_0 - E_1)/k_B T_m} \quad (39)$$

$$\frac{J_{b+}}{J_{b-}} = \frac{k_{43}k_{05}}{k_{34}k_{50}} = e^{-(E_0 - E_2)/k_B T_m} \quad (40)$$

$$\frac{J_{c+}}{J_{c-}} = \frac{k_{43}k_{32}k_{10}k_{05}}{k_{34}k_{23}k_{01}k_{50}} = e^{-(E_1 - E_2)/k_B T_m} \quad (41)$$

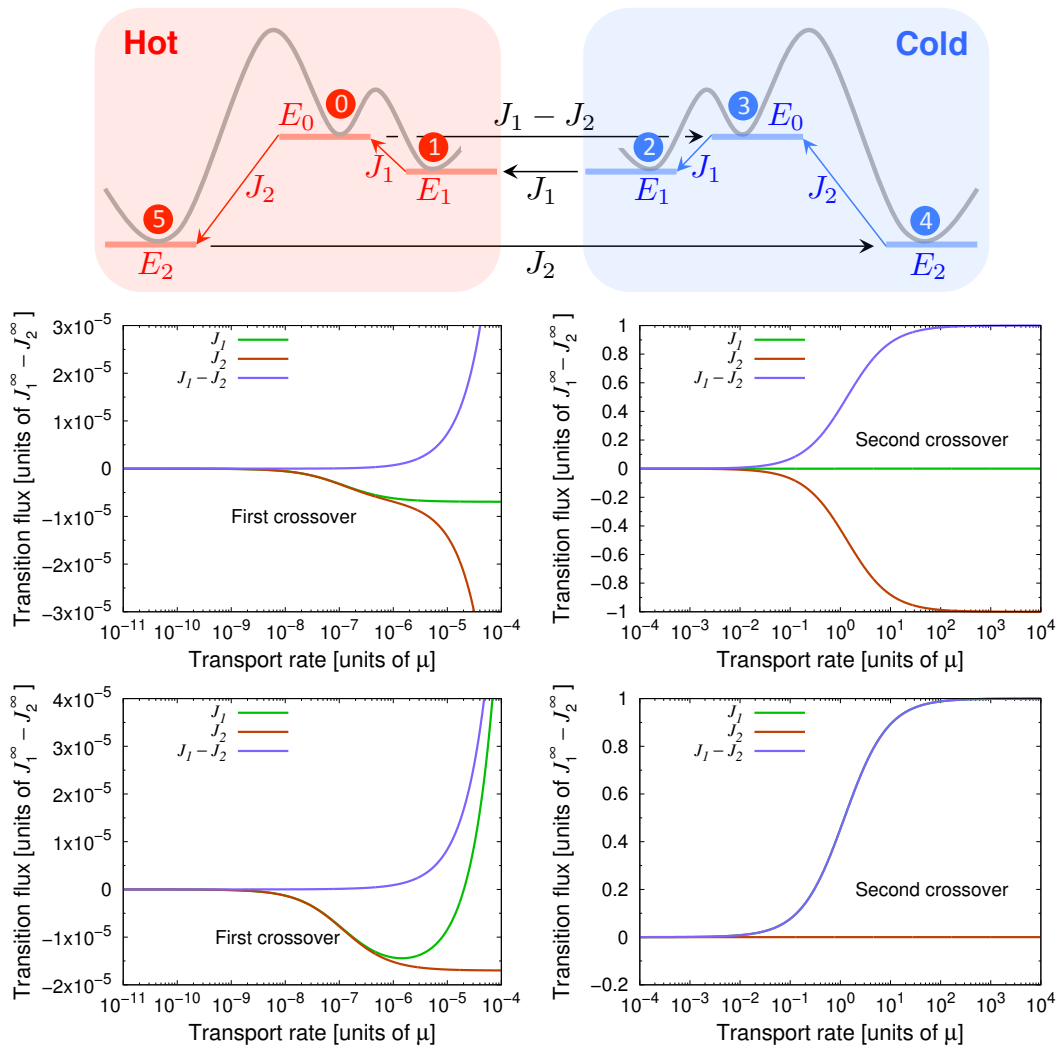


Figure 12: **The steady-state populations are sustained by steady currents, which circulate in different subgraphs in the first and second crossover regimes.** Fluxes as a function of the mobility rate. Top graphs: ultra-destabilisation scenario, $\Delta E_1 = 30$ kJ/mol, $\Delta E_2 = 0$. A steady clockwise flux in the b cycle ($J_1 - J_2 = -J_2 > 0$) sustains as $k_D \rightarrow \infty$ a ultra-high population of the low-energy state E_2 and an ultra-low population of the high-energy state E_1 . Bottom graphs, ultra-stabilisation scenario, $\Delta E_1 = 0$, $\Delta E_2 = 30$ kJ/mol. In this case, steady counterclockwise flux in the a cycle ($J_1 - J_2 = J_2 > 0$) sustains as $k_D \rightarrow \infty$ an ultra-low population of the low-energy state E_2 and a ultra-high population of the high-energy state E_1 . Clockwise from top to bottom: $\Delta E_1 = 0$ and varying $\Delta E_2 \in [0, 30]$ kJ/mol. $\Delta E_1 = 10$ kJ/mol and varying $\Delta E_2 \in [0, 30]$ kJ/mol (the blue dashed line corresponds to $\Delta E_2 = \Delta E_1 = 10$ kJ/mol). $\Delta E_2 = 0$ kJ/mol and varying $\Delta E_1 \in [0, 30]$ kJ/mol. Varying $\Delta E_1 = \Delta E_2 \in [0, 30]$ kJ/mol. Parameters are $\eta_1 = 29.34$, $\eta_2 = 1.945$, $E_0 = 19$ kJ/mol, $E_1 = 13.6$ kJ/mol, $E_2 = 3.1$ kJ/mol, corresponding to the average values for the two furanose and pyranose enantiomers measured from equilibrium NMR experiments.

where

$$\frac{1}{T_m} = \frac{1}{T_1} - \frac{1}{T_2} \quad (42)$$

$$J_a = J_{a+} - J_{a-} = J_{a-} [e^{(E_0-E_1)/k_B T_m} - 1] \geq 0 \quad (43)$$

$$J_b = J_{b+} - J_{b-} = J_{b-} [e^{-(E_0-E_2)/k_B T_m} - 1] \leq 0 \quad (44)$$

$$J_c = J_{c+} - J_{c-} = J_{c-} [e^{-(E_1-E_2)/k_B T_m} - 1] \leq 0 \quad (45)$$

The above inequalities follow directly from the strict positivity of one-way cycle fluxes, which are rational functions of products of rates.¹⁹

Much insight can be gained by inspecting the *transition* fluxes, $J_{ij} = -J_{ji}$, between any two neighboring states in the diagram. These are simply given by the sum (including the appropriate sign) of cycle fluxes for those cycles that comprise the link ij (from i to j). For example, the flux between the nodes representing the linear species from hot to cold is $J_{03} = J_a - J_b$. It should be noted that, at least in principle, transition fluxes are observable, while cycle fluxes are not.

In general, if a network comprises N nodes and M links, there are $N_J = M - N + 1$ independent transition fluxes. In our case, $M = 7$, $N = 6$, hence $N_J = 2$. These can be conveniently identified as

$$J_1 = J_a + J_c \quad (46)$$

$$J_2 = J_b + J_c \quad (47)$$

so that all transition fluxes are determined as $J_{32} = J_{21} = J_{10} = J_1$, $J_{05} = J_{54} = J_{43} = J_2$, $J_{03} = J_1 - J_2$. Note that the second law of thermodynamics is obviously not violated in the non-equilibrium steady state, as the net energy flux still proceeds from the hot to the cold box. Recalling the definition of transition fluxes and Eqs. (46), (47), the total heat flux from

the hot source to the cold one reads

$$\begin{aligned}
\dot{Q} &= E_0 J_{03} + E_1 J_{12} + E_2 J_{54} \\
&= (E_0 - E_1) J_1 - (E_0 - E_2) J_2 \\
&= (E_2 - E_1) J_2 + (E_0 - E_1) (J_1 - J_2) \geq 0
\end{aligned} \tag{48}$$

where the last passage follows from the definitions of cycle fluxes (43), (44) and (45), which imply $J_2 \leq 0$, $J_1 - J_2 \geq 0$. The currents circulating in the system in the limit $k_D \rightarrow \infty$ are illustrated in Fig. 13.

Rate of entropy production and energy dissipation

It is interesting to compute the rate of entropy production and to relate it to the non-equilibrium stabilisation sustained by steady currents in the system, as illustrated in the main text. The rate of entropy production can be computed as²⁰

$$\dot{S} = \frac{1}{2} \sum_{i,j=0}^5 J_{ji} \log \left(\frac{k_{ji} x_j}{k_{ij} x_i} \right) \tag{49}$$

where $J_{ji} = k_{ji} x_j - k_{ij} x_i$ is the transition flux from node j to node i . Recalling Eqs. (39), (40) and (41) and taking into account the definitions of the operational fluxes J_1 and J_2 , Eqs. (46) and (47), it is not difficult to see that Eq. (49) simplifies to

$$\dot{S} = \frac{1}{k_B T_m} [J_1 (E_0 - E_1) - J_2 (E_0 - E_2)] \tag{50}$$

where T_m is the reduced temperature defined by Eq. (42). Direct inspection of Eq. (48), shows that the rate of entropy production is proportional, as it should, to the net heat flux

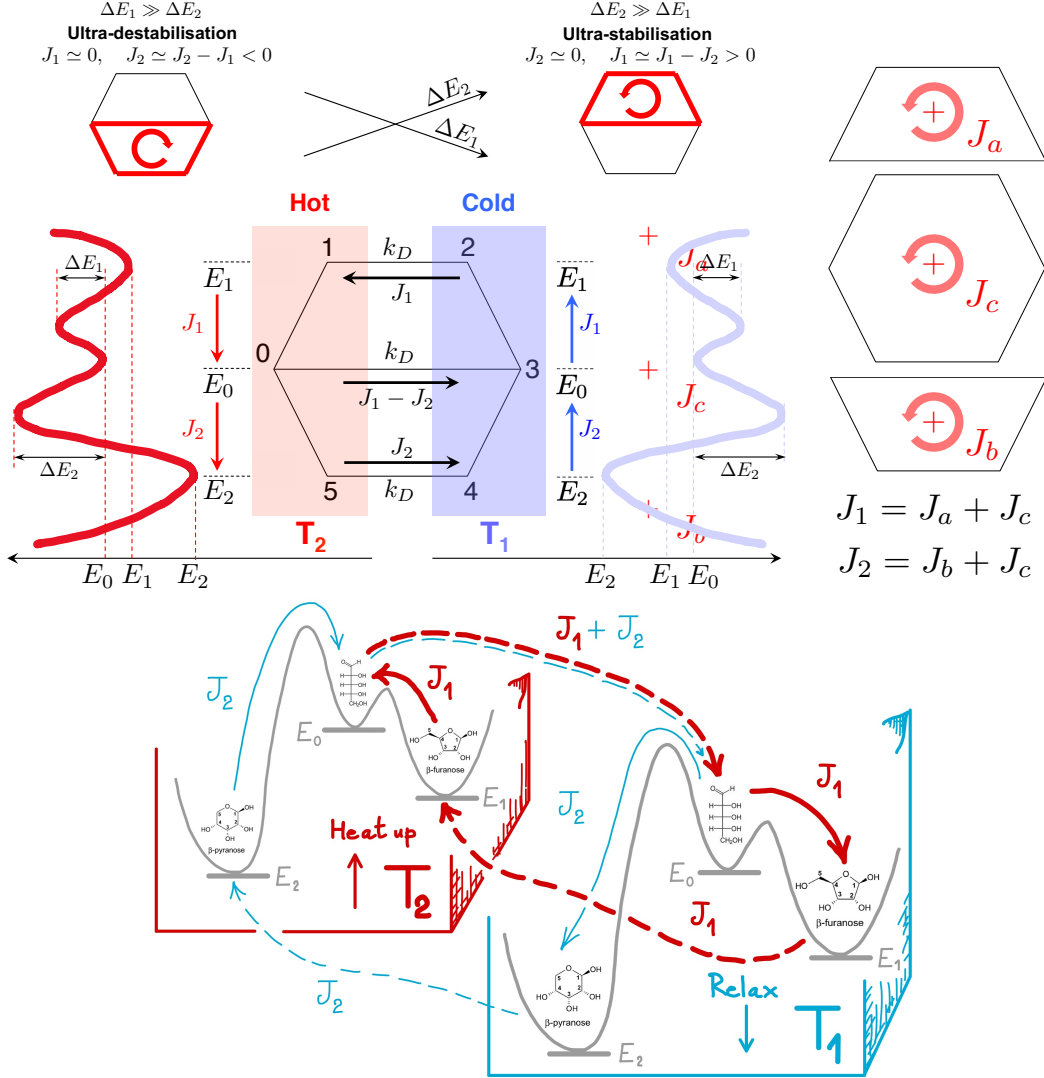


Figure 13: **Coarse-grained ribose isomerisation network in a steady temperature gradient.** Top: as one of the linear-to-cycle transition becomes faster than the other, the corresponding barrier becoming smaller, its population is boosted as a result of sustained non-equilibrium currents, as shown within the corresponding sub-graphs. Bottom left: scheme of the network with the corresponding energy landscapes and transition fluxes. The latter can be conveniently expressed in terms of two independent linear combinations of the three cycle fluxes J_a , J_b and J_c (right). The direction of the transition fluxes shown reflects the choice made for their definition, that is, an arrow from i to j stands for the $i \rightarrow j$ flux (which can be either positive or negative). Bottom. Illustration of the steady system of currents that circulate in the system in the case of ultra-stabilisation, $\Delta E_2 \gg \Delta E_1$. Dashed arrows denote transport, solid lines stand for chemical transformations. The current J_2 is much smaller than J_1 in the fast transport limit, $k_D \gg k_D^{*[2]}$. For example, for $\Delta E_2 = 30$ kJ/mol and $\Delta E_1 = 0$, $J_2/J_1 \simeq 6.5 \times 10^{-5}$, while for $\Delta E_2 = 20$ kJ/mol and $\Delta E_1 = 5$ kJ/mol, $J_2/J_1 \simeq 1.2 \times 10^{-2}$

flowing from the hot reservoir to the cold one, namely

$$k_B \dot{S} = \left(\frac{1}{T_1} - \frac{1}{T_2} \right) \dot{Q} \quad (51)$$

From the analysis of fluxes reported in the previous section, it is not difficult to realise that (see again Fig. 7) and Fig. 5 in the main text) in general the following equalities hold (at any time)

$$\begin{aligned} J_1 &= k_D(x_2 - x_1) \\ J_2 &= k_D(x_5 - x_4) \end{aligned} \quad (52)$$

Using Eqs. (25) and observing that $\alpha_{22} = \alpha_{21}$ and $\alpha_{25} = \alpha_{24}$ (see again the topology of the spanning trees shown in Fig. 7), we get

$$\begin{aligned} J_1 &= k_D \frac{(x_2^{\text{int}} - x_1^{\text{int}})k_D^{*[2]}k_D + (x_2^{\text{eq}} - x_1^{\text{eq}})k_D^{*[1]}k_D^{*[2]}}{k_D^2 + k_D^{*[2]}k_D + k_D^{*[1]}k_D^{*[2]}} \\ J_2 &= k_D \frac{(x_5^{\text{int}} - x_4^{\text{int}})k_D^{*[2]}k_D + (x_5^{\text{eq}} - x_4^{\text{eq}})k_D^{*[1]}k_D^{*[2]}}{k_D^2 + k_D^{*[2]}k_D + k_D^{*[1]}k_D^{*[2]}} \end{aligned} \quad (53)$$

Plugging Eqs. (53) in the definition of the rate of entropy production, Eq. (50), the latter can be cast in the particularly transparent form

$$\dot{S} = \frac{\dot{S}_\infty k_D^2 + \dot{S}_{\text{int}} k_D k_D^{*[2]}}{k_D^2 + k_D^{*[2]}k_D + k_D^{*[1]}k_D^{*[2]}} \simeq \begin{cases} \dot{S}_{\text{int}} \frac{k_D}{k_D + k_D^{*[1]}} & \text{for } k_D \ll k_D^{*[2]} \\ \frac{\dot{S}_\infty k_D + \dot{S}_{\text{int}} k_D^{*[2]}}{k_D + k_D^{*[2]}} & \text{for } k_D \gg k_D^{*[1]} \end{cases} \quad (54)$$

In particular, we get the following simple asymptotic forms,

$$\dot{S} \simeq \begin{cases} \dot{S}_{\text{int}} \left(\frac{k_D}{k_D^{*[1]}} \right) & \text{for } k_D \rightarrow 0 \\ \dot{S}_\infty \left[1 - \frac{k_D^{*[2]}}{k_D} \left(1 - \frac{\dot{S}_{\text{int}}}{\dot{S}_\infty} \right) \right] & \text{for } k_D \rightarrow \infty \end{cases} \quad (55)$$

The limit of vanishing transport rate

In the limit $k_D \rightarrow 0$, we see from Eq. (52) that the two operational fluxes read

$$\begin{aligned} J_1 &\simeq \frac{1}{2}k_D (P_{E_1}^{\text{eq}}(T_1) - P_{E_1}^{\text{eq}}(T_2)) \\ J_2 &\simeq \frac{1}{2}k_D (P_{E_2}^{\text{eq}}(T_2) - P_{E_2}^{\text{eq}}(T_1)) \end{aligned} \quad (56)$$

where we have used Eqs. (14). Hence, we have from expression (50)

$$\dot{S} = \frac{1}{k_B T_m} [(E_0 - E_1) (P_{E_1}^{\text{eq}}(T_1) - P_{E_1}^{\text{eq}}(T_2)) - (E_0 - E_2) (P_{E_2}^{\text{eq}}(T_2) - P_{E_2}^{\text{eq}}(T_1))] k_D \quad (57)$$

We see that the entropy production rate increases linearly with the transport rate k_D at small values of the latter. The expression (57) can be simplified further and made more transparent by expanding it in powers of $\Delta T/T_M$, where $T_M = (T_1 + T_2)/2$ (≈ 0.85 with the choice of temperatures considered in this work, and recalling that $P_{E_0}^{\text{eq}}(T_i) \ll P_{E_1}^{\text{eq}}(T_i), P_{E_2}^{\text{eq}}(T_i), i = 1, 2$. After a straightforward calculation, we get

$$\dot{S} = \frac{1}{2}P_{E_1}^{\text{eq}}(T_M)P_{E_2}^{\text{eq}}(T_M) \left(\frac{E_2 - E_1}{k_B T_M}\right)^2 \left(\frac{\Delta T}{T_M}\right)^2 k_D + \mathcal{O}(k_D^2, \Delta T^3) \quad (58)$$

Fig. 14 shows the trend of the entropy production rate \dot{S} as a function of the transport rate k_D for different choices of the barriers ΔE_1 and ΔE_2 . It can be appreciated that the system dissipates more the faster the transport, until a maximum dissipation rate is reached that depends only on the choice of the barriers and the imposed temperature gradient.

References

- (1) Dass, A. V. Stochastic Prebiotic Chemistry. Ph.D. thesis, Health, Biological Sciences and Chemistry of Life (SSBCV), 2018.
- (2) Zharkov, M. A. *History of Paleozoic salt accumulation*; Springer-Verlag: Berlin, 1981.

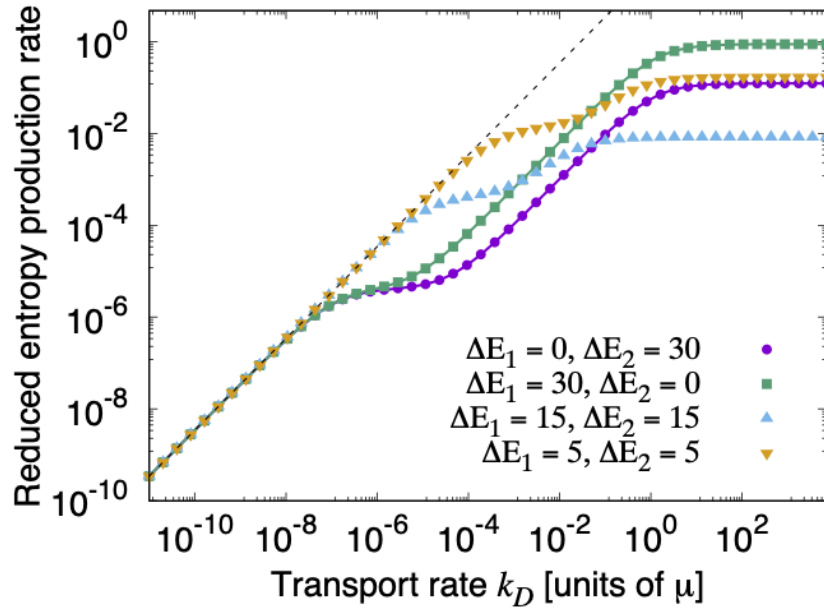


Figure 14: Plot of the reduced entropy production rate for different choices of the two barriers ΔE_1 and ΔE_2 . The solid lines are fits with the expression (54). The vanishing transport prediction (57) is shown explicitly as a dashed line. All other parameters are fixed as described in the main text at the values determined experimentally for the ribose isomerisation network.

- (3) Knauth, L. P. Salinity history of the Earth's early ocean [5]. *Nature* **1998**, *395*, 554–555.
- (4) De Ronde, C. E.; Channer, D. M.; Faure, K.; Bray, C. J.; Spooner, E. T. Fluid chemistry of Archean seafloor hydrothermal vents: Implications for the composition of circa 3.2 Ga seawater. *Geochimica et Cosmochimica Acta* **1997**, *61*, 4025–4042.
- (5) Rollinson, H. *Early Earth Systems: A Geochemical Approach*; Wiley-Blackwel, 2007.
- (6) Knauth, L. P. Temperature and salinity history of the Precambrian ocean: implications for the course of microbial evolution. *Palaeogeography, Palaeoclimatology, Palaeoecology* **2005**, *219*, 53–69.
- (7) Rimstidt, J. D. Quartz solubility at low temperatures. *Geochimica et Cosmochimica Acta* **1997**, *61*, 2553–2558.

- (8) Habicht, K. S.; Gade, M.; Thamdrup, B.; Berg, P.; Canfield, D. E. Calibration of sulfate levels in the Archean ocean. *Science* **2002**, *298*, 2372–2374.
- (9) Sumner, D. Y. Carbonate precipitation and oxygen stratification in late Archean seawater as deduced from facies and stratigraphy of the gamohaam and frisco formations, transvaal supergroup, South Africa. *American Journal of Science* **1997**, *297*, 455–487.
- (10) Crowe, S. A.; Jones, C. A.; Katsev, S.; Magen, C.; O'Neill, A. H.; Sturm, A.; Canfield, D. E.; Haffner, G. D.; Mucci, A.; Sundby, B.; Fowle, D. A. Photoferrotrophs thrive in an Archean Ocean analogue. *Proceedings of the National Academy of Sciences of the United States of America* **2008**, *105*, 15938–15943.
- (11) Holland, H. D.; Lazar, B.; McCaffrey, M. Evolution of the atmosphere and oceans. *Nature* **1986**, *320*, 27–33.
- (12) Busigny, V.; Planavsky, N. J.; Jézéquel, D.; Crowe, S.; Louvat, P.; Moureau, J.; Villotier, E.; Lyons, T. W. Iron isotopes in an Archean ocean analogue. *Geochimica et Cosmochimica Acta* **2014**, *133*, 443–462.
- (13) Douville, E.; Charlou, J. L.; Oelkers, E. H.; Bienvenu, P.; Jove Colon, C. F.; Donval, J. P.; Fouquet, Y.; Prieur, D.; Appriou, P. The rainbow vent fluids (36 °, 14' N, MAR): the influence of ultramafic rocks and phase separation on trace metal content in Mid-Atlantic Ridge hydrothermal fluids. *Chemical Geology* **2002**, *184*, 37–48.
- (14) Hawkes, J. A.; Connelly, D. P.; Gledhill, M.; Achterberg, E. P. The stabilisation and transportation of dissolved iron from high temperature hydrothermal vent systems. *Earth and Planetary Science Letters* **2013**, *375*, 280–290.
- (15) Gallant, R. M.; Von Damm, K. L. Geochemical controls on hydrothermal fluids from the Kairei and Edmond Vent Fields, 23 °-25 °S, Central Indian Ridge. *Geochemistry, Geophysics, Geosystems* **2006**, *7*.

- (16) Canfield, D. E. The early history of atmospheric oxygen: Homage to Robert M. Garrels. *Annu. Rev. Earth Planet. Sci* **2005**, *33*, 1–36.
- (17) Kappler, A.; Pasquero, C.; Konhauser, K. O.; Newman, D. K. Deposition of banded iron formations by anoxygenic phototrophic Fe(II)-oxidizing bacteria. *Geology* **2005**, 865–868.
- (18) Ricardo, A.; Carrigan, M. A.; Olcott, A. N.; Benner, S. A. Borate Minerals Stabilize Ribose. *Science* **2004**, *303*, 196.
- (19) Hill, T. L. *Free Energy Transduction and Biochemical Cycle Kinetics*; Springer-Verlag New York, 1989.
- (20) Schnakenberg, J. Network theory of microscopic and macroscopic behavior of master equation systems. *Reviews of Modern Physics* **1976**, *48*, 571–585.